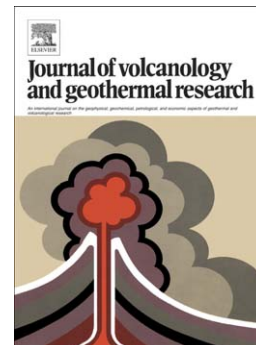| Title	Quantitative geometric description of fracture systems in an andesite lava flow using terrestrial laser scanner data
Author(s)	Massiot, Cécile; Nicol, Andrew; Townend, John; McNamara, David D.; Garcia-Sellés, David; Conway, Chris E.; Archibald, Garth
Publication Date	2017-06-03
Publication Information	Massiot, Cécile, Nicol, Andrew, Townend, John, McNamara, David D., Garcia-Sellés, David, Conway, Chris E., & Archibald, Garth. (2017). Quantitative geometric description of fracture systems in an andesite lava flow using terrestrial laser scanner data. Journal of Volcanology and Geothermal Research, 341, 315-331. doi: http://dx.doi.org/10.1016/j.jvolgeores.2017.05.036
Publisher	Elsevier
Link to publisher's version	https://doi.org/10.1016/j.jvolgeores.2017.05.036
Item record	http://hdl.handle.net/10379/6727
DOI	http://dx.doi.org/10.1016/j.jvolgeores.2017.05.036

Accepted Manuscript

Quantitative Geometric Description of Fracture Systems in an Andesite Lava
Flow Using Terrestrial Laser Scanner Data

Cécile Massiot, Andrew Nicol, John Townend, David D. McNamara,
David García-Sellés, Chris E. Conway, Garth Archibald

Please cite this article as: Massiot, Cécile, Nicol, Andrew, Townend, John, McNa-
mara, David D., García-Sellés, David, Conway, Chris E., Archibald, Garth, Quan-
titative Geometric Description of Fracture Systems in an Andesite Lava Flow Using
Terrestrial Laser Scanner Data, *Journal of Volcanology and Geothermal Research* (2017),
doi:10.1016/j.jvolgeores.2017.05.036

Quantitative Geometric Description of Fracture Systems in an Andesite Lava Flow Using Terrestrial Laser Scanner Data

Cécile Massiot[a,d,*], Andrew Nicol[b], John Townend[a], David D. McNamara[c,d], David García-Sellés[e], Chris E. Conway[f,a], Garth Archibald[d]

[a]*Victoria University of Wellington, PO Box 600, Wellington 6012, New Zealand*
[b]*University of Canterbury, Christchurch, New Zealand*
[c]*Earth and Ocean Sciences, School of Natural Sciences, National University of Ireland, University Road, Galway, Ireland*
[d]*GNS Science, Avalon, PO Box 30-368, Lower Hutt 5040, New Zealand*
[e]*University of Barcelona, Barcelona, Spain*
[f]*Department of Geology and Paleontology, National Museum of Nature and Science, 4-1-1, Amakubo, Tsukuba, Ibaraki 305-0005, Japan*

Abstract

Permeability hosted in andesitic lava flows is dominantly controlled by fracture systems, with geometries that are often poorly constrained. This paper explores the fracture system geometry of an andesitic lava flow formed during its emplacement and cooling over gentle paleo-topography, on the active Ruapehu volcano, New Zealand. The fracture system comprises column-forming and platy fractures within the blocky interior of the lava flow, bounded by autobreccias partially observed at the base and top of the outcrop. We use a terrestrial laser scanner (TLS) dataset to extract column-forming fractures directly from the point-cloud shape over an outcrop area of $\sim$3090 m^2. Fracture processing is validated using manual scanlines and high-resolution panoramic photographs. Column-forming fractures are either steeply or gently dipping with no preferred strike orientation. Geometric analysis of fractures derived from the TLS, in combination with virtual scanlines and trace maps, reveals that: (1) steeply dipping column-forming fracture lengths follow a scale-dependent exponential or log-normal distribution rather than a scale-independent power-law; (2) frac-

---

*Corresponding author
URL:* `c.massiot@gns.cri.nz` (Cécile Massiot)

ture intensities (combining density and size) vary throughout the blocky zone but have similar mean values up and along the lava flow; and (3) the areal fracture intensity is higher in the autobreccia than in the blocky zone. The inter-connected fracture network has a connected porosity of $\sim 0.5\,\%$ that promote fluid flow vertically and laterally within the blocky zone, and is partially connected to the autobreccias. Autobreccias may act either as lateral permeability connections or barriers in reservoirs, depending on burial and alteration history. A discrete fracture network model generated from these geometrical parameters yields a highly connected fracture network, consistent with outcrop observations.

Highlights:

- fracture orientation and density from a TLS 3-D point cloud in an andesitic lava flow

- column-forming fractures are oriented parallel or perpendicular to the brecciated base

- exponential length distribution, and $\sim 0.5\,\%$ connected fracture porosity assuming a $2\,\text{mm}$ mean aperture

- discrete fracture network models from measured geometries yield high connectivity

1. Introduction

Numerous geothermal, groundwater, CO_2 storage, radioactive storage, and more recently hydrocarbons reservoirs are hosted in lava flows (Custodio, 2007; Feng, 2008; Bertani, 2016). In these reservoirs, fluid flow is inferred to be controlled by fractures and faults, but the identification and geometric description

2

of permeable fracture networks often remains problematic (Arnórsson, 1995; Chen et al., 2001; Nemčok et al., 2007).

Fracture morphologies in lava flows have been extensively studied in basalts (e.g., DeGraff & Aydin, 1987; Schaefer & Kattenhorn, 2004; Hetényi et al., 2011; Vye-Brown et al., 2013) and less frequently in andesites (Doyuran et al., 1993; Deng et al., 1995; McCaffrey et al., 2003; Spörli & Rowland, 2006; Conway et al., 2015). Lava flows commonly have massive and fractured interiors, surrounded by autobreccias caused by mechanical breakage (Bonnichsen & Kauffman, 1987). The most prominent fracture types in the flow interior are column-forming joints, generated by the thermal stresses associated with cooling of the lava flow from the margins to the interior by contact with water or the atmosphere (DeGraff & Aydin, 1987, 1993; Lore et al., 2000). Fracture geometries depend on multiple environmental and lithological parameters including composition, weathering, cooling rate, morphology, paleo-topography, and crystal size (Grossenbacher & McDuffie, 1995; Karpuz & Paşamehmetoğlu, 1997; Custodio, 2007; Kattenhorn & Schaefer, 2008; Hetényi et al., 2011). Among other factors, the higher silica content of andesites (57–63 wt.% SiO_2) than basalts (45–57 wt. % SiO_2), associated with different cooling rates, may produce different fracture distributions (Forbes et al., 2014). The large range of silica content in andesites may also create variability in the fracture systems between different andesite lava flows.

Fracture systems in lava flow-hosted reservoirs result from the initial emplacement of the lava as well as subsequent interaction between tectonic, thermal, and hydrothermal processes (Fournier, 1998; Gudmundsson et al., 2001; Nemčok et al., 2004; Hetényi et al., 2011). The Rotokawa geothermal reservoir located in the Taupo Volcanic Zone (TVZ), New Zealand, is an example of one such andesite-hosted geothermal reservoir, in which the hydrothermally altered andesites have a low porosity (4.4–16.3%) and high strength (unconfined compressive strength -UCS- of 70–211 MPa), and fluid flow is structurally controlled (Siratovich et al., 2014; McNamara et al., 2015). Although the importance of fractures for fluid flow in this geothermal field is widely accepted, the fracture

3

distributions throughout the reservoirs are poorly understood. Establishing a "baseline" for the fracture distribution formed during the lava flow emplacement is a critical step for improved targeting of permeable fractures in reservoirs.

Fracture models can help with the management of resources via analysis of preferential flow pathways. Discrete fracture network (DFN) models describe fluid flow processes through rock masses by stochastically generating fractures (Dershowitz & Einstein, 1988; de Dreuzy et al., 2013). DFNs rely on the input of fracture geometries (mainly orientation, size, frequency and aperture). A number of probability distributions of fracture size (length or radius) and density have been used to generate fracture network models in basaltic and andesitic reservoirs (Doyuran et al., 1993; Deng et al., 1995; Chen et al., 2001; Lee et al., 2010; Pollyea et al., 2014) reflecting the variability of fracture geometries in such lithologies.

Probability distributions of fracture geometries are typically estimated from 1-D scanlines in outcrop (Priest, 1993) and boreholes using image logs (e.g., Barton et al., 1995; Massiot et al., 2015a), or 2-D circular sampling in outcrops (Mauldon et al., 2001). Terrestrial laser scanner (TLS) datasets, also called terrestrial Lidar, allow a comprehensive fracture analysis of an entire outcrop in 3-D, which is therefore less subject to observation biases than scanlines or window samplings of limited sizes (though other specific biases have to be considered; Lato et al., 2010), and supports more reliable statistics on fracture geometries (Hodgetts, 2013). The large fracture datasets obtained from TLS are sometimes different from empirical relationships defined from scanlines, and TLS data may be more appropriate than scanlines for reservoir analogue studies (Pearce et al., 2011). TLS studies are increasingly applied to geoscientific questions (Abellan et al., 2016), including in volcanic settings (e.g., Massey et al., 2010; Nelson et al., 2011; Geyer et al., 2015; Nelson et al., 2015). Fracture delineation from TLS has been used for slope stability analysis (Deparis et al., 2008), fracture density statistics in sedimentary and plutonic formations (Jones et al., 2008; Rotevatn et al., 2009; Pearce et al., 2011), and input into reservoir simulations (Enge et al., 2007; Fabuel-Perez et al., 2010) or DFN models (Wilson

4

et al., 2011) in the hydrocarbon industry (see Hodgetts, 2013, and references therein). Fracture systems within lava flows have rarely been studied using TLS, focusing on basalt (Pollyea & Fairley, 2012) rather than andesite flows. Alternative structure-from-motion photogrammetry acquired from drones is becoming common for structural analysis of outcrop (Bemis et al., 2014), thanks to its low cost and ease of use. However, TLS datasets are still more accurate and suitable for the measurements of fracture geometries for reservoir applications at present than structure-from-motion photogrammetry (James & Robson, 2012; Hodgetts, 2013).

In this paper, we provide constraints for DFN models of a fracture system in an andesitic lava flow of the Ruapehu volcano, New Zealand, based on the analysis of a TLS dataset. We use the recently developed "Facets" methodology for extracting fractures from a TLS point cloud based solely on the shape of the outcrop (Dewez et al., 2016). We discuss the implications of the fracture geometries obtained from the TLS dataset for the permeability of andesite-hosted reservoirs, using synthetic DFN models.

2. Geological Setting

2.1. Ruapehu volcano, Central North Island of New Zealand

Ruapehu is New Zealand's largest active andesitic volcano, located at the southern end of the Taupo Volcanic Zone (TVZ) in the central North Island of New Zealand (Figure 1; Hackett & Houghton, 1989; Wilson et al., 1995). Ruapehu may be as old as 340 kyr (Tost & Cronin, 2015), but the exposed edifice was mainly constructed by basaltic-andesite to dacite lava effusion in the last 200 kyr (Gamble et al., 2003; Conway et al., 2016). Ruapehu is primarily composed of blocky lava flows and autobreccias, with 54–65 wt. % SiO_2 (Hackett & Houghton, 1989). Porphyritic andesite lavas of the Whakapapa Formation were emplaced between 10 and 4 ka and form much of the upper flanks of the volcano (Conway et al., 2015, 2016). Post-glacial lava flows such as those of the Whakapapa Formation have low height-to-width ratios (<1:10), are typically

5

<5 m thick, and are associated with autobreccias and welded spatter (Conway et al., 2015).

2.2. Description of the Happy Valley Outcrop

The present study focuses on a lava flow in "Happy Valley" located near the Iwikau Village ski field on the NNW flank of Ruapehu (Figure 1a). The Happy Valley flow is part of a Holocene low-volume coherent andesite lava flow that was emplaced on a relatively shallow slope gradient (∼10°) on the flanks of Ruapehu. As such, it is a representative site for constraining the fracture geometries and properties of Whakapapa Formation lavas, and similar sheet flows and autobreccias that make up the older formations at Ruapehu at mid-low elevations (<1600 m, Happy Valley's altitude) where the ice extent was limited. While the compositional range of Ruapehu lavas extends from ∼54–65 wt. % SiO_2, andesite lavas with ∼58–60 wt. % SiO_2 such as Happy Valley are the most common eruptive product (Price et al., 2012; Conway et al., 2016). Hackett & Houghton (1989) concluded that sheet lavas and associated autobreccias comprise ∼88 vol. % of the edifice. Other deposits that form the Ruapehu edifice include hyaloclastite breccias, pyroclastic rocks, alluvium, and debris avalanche deposits which likely have distinct fracture properties compared to the Happy Valley lava flow.

The Happy Valley outcrop is a ∼210 m-long section of a 4.5–21 m-thick, young (∼6 ka; Conway et al., 2016) lava flow of the Whakapapa Formation with 59 wt. % SiO_2 (Wysoczanski, 1989). The rock face predominantly presents the interior of a blocky andesite lava flow emplaced over low-angle topography (slope ∼10°; Figures 1b-c, 2a). The lava flow is underlain by a lower autobreccia (referred to as "breccia" in the remaining of the paper) which is intermittently observed. The upper breccia is mostly hidden by vegetation or eroded, and a 1–3 m-thick zone is observable in the northern part of the outcrop (see Section 4.3). The results presented here are representative of this "simple" configuration and do not take into account fracturing caused by lava-ice interactions (Conway et al., 2015), emplacement over a knob, variations in composition, faulting, or

6

other parameters as described by Hetényi et al. (2011).

Fractures studied in this outcrop are joints formed in mode I (opening only) during the emplacement and cooling of the lava flow at the ground surface (De-Graff & Aydin, 1987; Pollard & Aydin, 1988), and are referred to as "fractures" in the general sense of a discontinuity. Two main types of fractures are observed in the Happy Valley outcrop:

1. Column-forming fractures: most common fractures, which delimit columns of polygonal cross-section, roughly perpendicular to the top and base of the lava flow. These fractures are straight to curved (Figure 3a), and divide the rock mass into blocks (Figure 1c.

2. Platy fractures: closely-spaced fractures, spatially clustered, sub-parallel to each other, along which the lava breaks into flaky sheets or smaller platy fragments (mm-cm-thick, 1–100 cm across; Figure 3a) as described by Lescinsky & Fink (2000) and Conway et al. (2015). Platy fractures are generally subhorizontal in the central zones of the flow and moderately to steeply inclined in the upper zones. They form along planes of weakness parallel to aligned crystals, and thin, vesicle-rich layers (Conway et al., 2015).

3. TLS Processing, Fracture Processing and Fracture Analysis

3.1. Data Acquisition

TLS devices emit and receive laser pulses at predefined vertical and horizontal angular intervals. The resulting high-density 3-D point cloud is a measurement of the location (x, y, z) and backscattered energy of each pulse reflected off a surface (Pfeifer & Briese, 2007; Buckley et al., 2008). By rotating both horizontally and vertically the TLS can survey the target surface with an array of millions of measurements. In this study, TLS scans were acquired using the Riegl LMS-Z420I instrument from three positions precisely located by Leica series 1200 RTK GPS measurements, with one station mounted directly on the TLS and two additional stations located on top of the outcrop (Appendix A).

The acquisition of TLS scans from several locations and angles to the target limits blind areas in the final combined point cloud, such as behind buildings that the laser rays cannot directly access, and more accurately characterises the target surface by reducing the line-of-sight and distance bias (Buckley et al., 2008). TLS point cloud resolution is $\sim$4–5 cm after processing (Appendix A). Georeferenced photographs were also taken from each TLS location. While photographs can be visualised in 3-D after being draped over the TLS point cloud, they lack the resolution to show fine details ($<$1 cm).

Three high-resolution panoramic photographs were acquired with a Gigapan system from different angles to cover the entire outcrop studied, providing details at the centimetric to millimetric scale (Gigapan, 2016, Figures 2a and 3a). As they are not georeferenced, Gigapan photographs were not draped over the point cloud, but their higher resolution complements the georeferenced pictures.

The location, length, and terminating relationships of 192 column-forming fractures were measured manually along a 100 m-long scanline near the base of the outcrop (Figure 2a, Table 1). Changes of facies (blocky or breccia) were also noted. The scanline is made at different heights near the base of the outcrop, and with variable trend and plunge, which ensures sampling of fractures at a range of angles to the flow direction. In addition to the scanline *per se*, the orientation and spacing of two zones of closely-spaced platy fractures intersecting, and located near the scanline, respectively, were measured. While the scanline does not cover the whole area measured by the TLS, it offers detailed insights into the relationships between fractures, and a calibration for the TLS fracture delineation.

3.2. Fracture delineation From the TLS Point Cloud

Several approaches have been developed to extract fractures and their properties from a TLS point cloud using various computational strategies and degrees of user interaction. These approaches aim to delineate fracture traces perpendicular to, or planes sub-parallel to exposures. Fracture traces or faces can be delineated manually on photographs before (Nelson et al., 2011) or after draping

8

over the point cloud (referred to as digital outcrop model, DOM; Buckley et al., 2008; Hardebol & Bertotti, 2013). The generation of a DOM requires the point cloud to be meshed, which can be a computationally complex task where there is significant outcrop topography. Methods for automatically sampling fracture traces have been developed (Umili et al., 2013), but the fracture orientations in such cases are not well constrained. Fully- or semi-automatic detection of fracture faces typically depends on the *a priori* definition of fracture sets of specific orientations, and operate with or without meshing of the point cloud (e.g., Olariu et al., 2008; García-Sellés et al., 2011; Gigli & Casagli, 2011; Riquelme et al., 2014). The ability of these techniques to detect fractures is limited in the absence of fracture populations of specific orientations, as is the case in lava flows. Pollyea & Fairley (2011) used the higher roughness occurring at the fracture edges to detect fracture densities, but this technique does not provide fracture orientation and size.

In this work, fractures are extracted directly from the shape of the 3-D point cloud TLS dataset, using the Facets plugin in CloudCompare (Dewez et al., 2016; CloudCompare, 2016), as detailed in Appendix A and Figure 4. Fractures are defined by portions of the point cloud that are approximatively coplanar (Figure 5a, Table A.1. The resulting fracture dataset contains the geometry of the planes forming the outcrop: the XYZ coordinates in the centre of each plane, together with the orientation and size (length, height, area) of the locally fitted plane. Overall, 3403 fractures covering an area of $\sim$3090 m^2 were delineated from the TLS point cloud.

Fracture orientations extracted from the TLS, and measured by hand, only differ by a few degrees in both dip magnitude and dip (Appendix A), a discrepancy consistent with the accuracies of TLS reported by Sturzenegger & Stead (2009a) and hand-held compass measurements.

3.3. Sampling Bias

Both the scanline measurements and the fracture dataset extracted from the TLS are affected by the under-sampling of the smallest fractures and the low

9

probability of intersection of the scarce larger fractures with the outcrop face (Pickering et al., 1995; Priest, 2004).

On the scanline, fractures <0.05 m-long were not recorded. The length was fully measured when the terminations were ∼3.5 m above, and 0.5–1.5 m below the scanline (depending on the height of the scanline above ground). The longest fracture (11.6 m) is sub-horizontal and was not affected by the sampling bias. Fracture length where one or both terminations were beyond the scanline swath are referred to as censored, and are thus longer than the reported measurement (Pickering et al., 1995).

The TLS-processed dataset contains only column-forming fractures. The detection of long fractures by the TLS is only affected by the height of the outcrop and location in line-of-sight (Buckley et al., 2008). The fracture processing extracts planes bounding the point subsets (Figure 5b), which limits the bias related to the measurement of chords to fractures instead of the fracture length itself (f-bias in Priest, 2004). Fractures with length <0.2 m were not resolved from the TLS point cloud (Appendix A). The centimetre-scale relief of column-forming fracture's growth increments visible on panoramic photographs is too small to be captured by the TLS (Appendix A, Figure A.1). Similarly, in-plane fractures that do not exhibit any 3-D relief are not resolved (Figures 3, A.1). Manual observations and investigation of Gigapan panoramas showed that this sampling bias is limited. Changes of facies (blocky lava and breccia), are also not detected by the TLS processing (Figure 3). The platy fractures are small and non-planar: they are not resolved by the TLS and are fitted collectively by a single plane (Figure 3).

3.4. Fracture Analysis Method

The inputs to discrete fracture network (DFN) models are probability distributions of fracture orientations, lengths, intensities (which combine fracture density and size), terminations, and apertures (Berkowitz, 2002). The steps used in this study to analyse fractures are summarised in Figure 4. We adopt the fracture density nomenclature "P_{ij}" commonly used in DFN modelling which

10

jointly describes the dimensionality of the sampling region (i) and the dimensionality of the fracture property (j) (Dershowitz & Herda, 1992).

Fracture orientation is analysed directly from the results of the TLS processing and scanline measurements (Figure 2c-d). The spatial distribution of fracture area is presented in Figure 2e. To assess the variability of fracture density within the outcrop, we evaluate P_{10}, the number of fractures intersected per unit length of scanline,along a series of virtual scanlines through the TLS-processed dataset at 10 cm intervals in two orthogonal directions. Sub-horizontal scanlines parallel to the brecciated base (dipping $\sim 10°$) measure P_{10} from the base to the top of the lava flow, whereas sub-vertical scanlines perpendicular to the brecciated base (dipping $\sim 84°$) measure P_{10} upflow to downflow. The calculations are made with the "Stratigraphy" tool of SEFL software (Laubach et al., 2009; García-Sellés et al., 2016). P_{10} values are affected by the shape of the outcrop, so we present results for zones which are sufficiently wide, high, and planar, namely zones 2, 4, 6, and 8 illustrated in Figure 7. We include in the analysis only those virtual scanlines that (1) are ≥ 10 m long, (2) intersect ≥ 10 fractures, and (3) are fully contained within the extent of the outcrop.

The P_{32} parameter (which expresses the summed area of fracture per volume of rock) is a measure of fracture intensity that combines both fracture density and size. P_{32} is a favoured intensity measure with which to characterise fracture systems, as it is invariant with respect to the distribution of fracture size and is scale independent; that is, it does not depend on the volume studied or the orientation of the measurements (Dershowitz & Einstein, 1988). P_{32} cannot be directly measured but can be derived from the P_{21} parameter (the summed length of fracture traces per area of rock):

$$P_{21} = L_f/A_t \tag{1}$$

where L_f is the total length of fracture traces measured on a surface of area A_t. P_{21} is classically measured on trace maps, which represent the intersection ("traces") of fractures with an outcrop (Figure 5b; see examples in Figure 13b). In this work, P_{21} is evaluated in two ways: (1) directly using the TLS-processed

11

fractures as the area used to sample fracture traces (although not perfectly planar); and (2) using virtual trace maps in the Fracman software. The first case assumes that TLS-processed fractures are tiled next to each other over a surface best-fitting the outcrop of area A_t:

$$P_{21} = \frac{\sum_i^n p_i/2}{A_t} \qquad (2)$$

with p_i being the perimeter of each fracture. The edge of each fracture is shared with a neighbouring fracture, so the total length of the segments is half the summed perimeter of each fracture. A_t is measured using Gocad software by fitting a surface to the point cloud.

In the second case, two series of virtual sections orthogonal to the outcrop face are generated, yielding virtual trace maps parallel and orthogonal to the lower breccia (i.e. sub-horizontal and sub-vertical). In this case, the A_t is measured as

$$A_t = l_{scanline} \cdot W \qquad (3)$$

with $l_{scanline}$ the length of the polyline formed at the the intersection between the outcrop surface and the trace map plane, and W a constant, fixed at $1\,\mathrm{m}$ based on visual inspections, which takes into account the sampling area of the shape of the outcrop.

Finally, the P_{32} parameter is proportional to P_{21}:

$$P_{32} = C_{32} \cdot P_{21} \qquad (4)$$

where C_{32} is related to the orientation distribution of the fractures (Wang, 2005). When all fractures have the same aperture, P_{33}, the volume of fractures per volume of rock (and thus the fracture porosity when reported as a percentage), is proportional to the fracture aperture a:

$$P_{33} = a \cdot P_{32} = a \cdot C_{32} \cdot P_{21} \qquad (5)$$

The probability distribution of fracture lengths is evaluated from the virtual trace maps parallel and orthogonal to the lower breccia. Fracture traces

12

sampled at the intersections of the TLS-processed fractures and the trace maps are "chords" to the actual fracture extent (Figure 5b). Fractures are modelled as penny-shaped disks, with a radius r and an aperture a. Probability distributions are fitted to the fracture traces, and then converted to a distribution of fracture radii in Fracman following Zhang et al. (2002). Three distributions commonly found to describe fracture lengths are tested (Bonnet et al., 2001): exponential, log-normal and power-law (Table 1). Fitting of these probability distributions to empirical cumulative density functions (CDFs) of fracture segments is evaluated with Kolmogorov–Smirnov (K–S) tests. A good fit is characterised by a low distance D between the estimated and empirical CDFs, and a high significance level. Finally, the fit of the complementary cumulative density function (CCDF; which is 1-CDF) to a linear model in log-linear and log-log plots, provides additional indication of the preferential fit to an exponential or a power-law distribution, respectively.

4. Results: Fracture Geometries

4.1. Orientation

Column-forming fractures have two main orientations: steeply dipping ($>55°$), and gently dipping ($<30°$), without a preferred strike orientation (Table 1). The scanline measurements reveal these two dip magnitude sets (Figure 6a) and the large variety of strike orientations (Figure 7b), regardless of the scanline trend which varies along the profile. The ratio of gently to steeply dipping fractures is 1:3, after correction for orientation sampling bias (Table 1; Terzaghi, 1965). Platy fractures observed on scanlines are gently dipping (10–25°). The correction for sampling bias involves the geometrical correction factor w based on the observed acute angle d between the scanline trend and the normal to the discontinuity: $w = 1/\cos d$. When d approaches $90°$ (fracture sub-parallel to the scanline trend), w becomes very large; in this case, a single point could dominate the distribution pattern. Following (Priest, 1993), with a fracture orientation accuracy of $\sim 3°$, we adopt a maximum value of $w=10$.

13

TLS-processed column-forming fractures are steeply dipping and strike sub-parallel to the outcrop, regardless of its orientation (Figure 7a), which confirms that there is no preferred strike orientation. Gently-dipping column-forming fractures are not well delineated by TLS processing because they are usually not in direct line-of-sight, and have insufficient 3-D relief (Figure 6a). The overall high density of fractures striking N–S relates to the large outcrop area with a $\sim$174°–354° strike orientation (zones 1 to 4). The varied strike orientation of the Happy Valley outcrop makes it suitable for extracting reliable statistics, similar to making scanlines in several directions as recommended by Priest (1993). The orientations of the steeply-dipping and gently-dipping column-forming fractures can thus be modelled using bivariate normal distributions (Table 1).

4.2. Connectivity (Scanlines) and Length (TLS and Scanlines)

The scanline dataset indicates that fractures are highly connected (fracture connectivity is not quantifiable from the TLS-processed dataset). Overall, 60% of the fractures with two observed tips observed terminate on another fracture at both ends, and an additional 30% on one end, yielding a termination probability of 75% (Table 1).

Scanline and TLS-processed datasets show a large range of fracture lengths about medians of 0.65 and 1 m, respectively (Table 1, Figure 6b). The TLS-processed fractures are longer in average than those on the scanline due to sampling biases (see Section 3.3). The longest fractures measured on the scanline and TLS-processed dataset ($\sim{\geq}5$ m) are steeply dipping ($>$70°). Moreover, numerous censored fractures (i.e. reported lengths are minimums) measured on the scanline are steeply dipping. By contrast, a long (11.6 m) sub-horizontal column-forming fracture was measured on the scanline, which was not detectable by the TLS processing.

Fracture radius follows either a negative exponential or a log-normal distribution. On sub-horizontal virtual trace maps parallel to the lower breccia, including a trace map at the manual scanline location, these two distributions have similar K–S test results (with median D of 0.07 and 0.08, and median

14

significance of 0.99 and 0.92, for the exponential and log-normal distributions, respectively), while power-law distributions always present poorer fits (median D of 0.15 and median significance of 0.31). Sub-vertical trace maps orthogonal to the lower breccia are under-constrained because of the limited number of fractures intersected along 8–15 m-long trace maps, but also have better fits to negative exponential and log-normal distributions than to power-law distributions. Sturzenegger & Stead (2009b) showed that the lower bound of the log-normal length distributions of TLS-processed fractures differs at different observation scales, and recommended using an exponential distribution. Given the limited range of observations of fracture radius at Happy Valley (1.5 orders of magnitude), we also favour the negative exponential distribution over the log-normal distribution because it has only one parameter, rather than the log-normal distribution which has two. Using an exponential instead of a log-normal distribution in conditions where both fit the data similarly well avoids over-parametrisation.

The exponential parameter $\frac{1}{\lambda}$ of the fracture radius evaluated from sub-horizontal trace maps (hence from fracture radius chords, Figure 5b) ranges between 0.4–0.6 m with a median of 0.5 m (Table A.3; parameters of the power-law and log-normal distribution fits are also included for comparison). There is no clear correlation between variations of probability distribution parameters and the location of the measurement within the lava-flow, either along flow or from base to top.

The preferred exponential distribution of fracture length (and thus radius) is confirmed by the scanline measurements. The complementary cumulative density functions (CCDFs) of fracture length measured on the scanline (with and without censored fractures), TLS-processed dataset, and on the subset of TLS-processed fractures in the manual scanline zone, all show a good fit to an exponential distribution (straight line in a log-linear plot; Figure 8). In addition, the exponential coefficients λ are similar for all these subsets (0.3–$0.5\,\mathrm{m}^{-1}$).

15

4.3. Variability of Fracture Area Between Breccia and Blocky Facies

Straight to curved columnar fractures either stop at the massive/breccia interface, or bifurcate in the mechanically weak and heterogeneous breccias (Figure 3). There are few exposures of the lower breccia at Happy Valley, but observations suggest that the fracture propagation is less affected by breccias with small clasts than with large clasts.

Fractures in the upper breccia zone, at the northern end of the outcrop, are smaller than in the underlying blocky zone, as revealed by the empirical probability density function (PDF) of fracture area (Figure 9c). While the median fracture area is similar in both the blocky and upper breccia zones (0.8 and $1.1\,\mathrm{m}^2$, respectively), only 4% of fractures in the breccia exceed $5\,\mathrm{m}^2$ in area, versus 15% in the blocky zone.

4.4. Linear Fracture Intensity: P_{10}

P_{10} measured along a series of virtual scanlines intersecting the TLS-processed dataset varies between 0.7–$1.7\,\mathrm{m}^{-1}$, with a mean of $1.2\pm0.1\,\mathrm{m}^{-1}$ (one standard deviation; Figure 10, Table 1). Sub-horizontal virtual scanlines show no clear relationship between the P_{10} value and location within the lava flow either from the base to the top of the blocky part of the outcrop, nor in the breccia intersected in zones 2 and 4 (Figure 7). There are no observed lateral variations of P_{10} between the up-flow and down-flow parts of the outcrop, as seen on sub-vertical virtual scanlines which sample the entire thickness of the outcrop. Steeply-dipping column-forming fractures measured along the manual scanline have a slightly higher P_{10} ($1.5\,\mathrm{m}^{-1}$) than the TLS-processed dataset, which reflects the additional sampling of short fractures.

4.5. Areal (P_{21}) and Volumetric (P_{32}) Intensity, and Fracture Porosity (P_{33})

The P_{21} of the steeply-dipping column-forming fractures for the blocky zone of this outcrop is estimated to be ~1.8–$2.0\,\mathrm{m}^{-1}$ (Table 1; Figure 11). The P_{21} value evaluated directly from the surface of the outcrop is 1.8–$2.0\,\mathrm{m}^{-1}$ in the blocky parts of the outcrop. P_{21} in the upper breccia of zones 2–4 is $2.6\,\mathrm{m}^{-1}$,

16

reflecting smaller fracture sizes than in the blocky region, and hence the higher total fracture edge length. The P_{21} derived from virtual trace maps parallel to the lower breccia is similar (1.7–$2.2\,\mathrm{m}^{-1}$) to those estimated from the surface of the outcrop, and does not exhibit any discernible variation related to the position in the outcrop (Figure 11). P_{21} values derived from sub-vertical trace maps orthogonal to the lower breccia are less constrained than those measured from trace maps parallel to the lower breccia, because of the lower number of intersected fractures, but have a similar range and median of P_{21} values. The two lowest P_{21} values, in zones 5 to 8, are measured in the narrowest part of the outcrop ($10\,\mathrm{m}$ high) and are thus the least reliable.

Calculation of the P_{33} parameter includes the C_{32} parameter and fracture aperture (Equation 5). Calculation of the C_{32} parameter requires the assumption that fracture sets define clusters with a mean orientation, or that orientation is isotropic (Wang, 2005). In the Happy Valley outcrop, fracture strikes lack a mean orientation. Although there are two sets of dip magnitude, we use the C_{32} value of 1.27 applicable to the isotropic case as an approximation (Wang, 2005). The corresponding P_{32} is 2.3–$2.5\,\mathrm{m}^{-1}$ (Equation 4). Sparse scanline measurements show that the fracture aperture is $\sim 2\,\mathrm{mm}$ (aperture is not measurable from the TLS as it is smaller than the point cloud resolution). The resulting P_{33} value for steeply dipping column-forming fractures is 0.0046–0.005, equivalent to $\sim 0.5\,\%$ fracture porosity (Figure 11).

5. Discussion

5.1. Column-forming Fracture Orientation and Size

Column-forming fractures at Happy Valley are either steeply- or gently-dipping, i.e. sub-perpendicular or sub-parallel to the lower breccia, without preferred strike orientation. These orientations are similar to outcrop observations away from the lateral margins in previous studies (DeGraff & Aydin, 1987; Schaefer & Kattenhorn, 2004), and numerical models (Lore et al., 2000, 2001; Kattenhorn & Schaefer, 2008) for basalt lava flows, and result from a cooling

17

front causing thermal stresses propagating inward from the base and the top of the lava flow.

TLS-processed fracture radii (modelled as disks) follow an exponential or a log-normal distribution; the exponential distribution is preferred here as it has only one parameter, and because it provides a good approximation of fracture length in the manual scanline and TLS-processed dataset. The robustness of this analysis is limited by the scale range of observations which spans less than two orders of magnitude. Fracture length measurements from thin sections would extend the range of observations to scales <1 cm and strengthen results from outcrop-scale observations, assuming that fractures at both scales result from the same processes.

The exponential fracture length distribution found in the Happy Valley andesite is consistent with the statistical analysis reported on moderately-weathered outcropping andesites (Sari et al., 2010), in the vicinity of mid-oceanic ridges in volcanic lava flows (Carbotte & Macdonald, 1994), and in other non-volcanic rocks (Cruden, 1977; Hudson & Priest, 1979; Priest & Hudson, 1981; Kulatilake et al., 1993; Aler et al., 1996). Exponential length distributions have been related to a growth process controlled by a uniform stress distribution (Dershowitz & Einstein, 1988), where the propagation of fractures is a Poissonian (random) process. In a lava flow, the thermal stress is controlled by the advance of the cooling from the outside to the inside of the lava flow; at a given time, the thermal stress is thus uniform in the direction parallel to the borders of the lava flow, and changing gradually from the border to the inside of the flow. This stress distribution is not uniform but is more gradual than in anisotropic stress distributions controlled by tectonic processes.

Exponential or log-normal fracture length distributions imply that the system has characteristic length scales, either λ or $(\bar{y}, y_\sigma)$, respectively (Table 1). In lava flows, fracture propagation is limited by the breccias at the boundaries of the flow, and the characteristic scales may thus relate to the dimensions of the lava flow (thickness, width and length). The length of column-forming fractures perpendicular to the lava flow direction has an upper bound at the

18

thickness of the lava flow (5–21 m), which is reflected in the 10 m maximum length measured in the TLS-processed dataset. The length of column-forming fractures is further restricted by gently-dipping platy fractures that arrest or deflect column-forming fractures. Column-forming fractures parallel to the lower breccia (gently dipping) tend to be shorter than those perpendicular to the lower breccia, although one 12 m-long sub-horizontal fracture parallel to flow-banding has been measured on the manual scanline. In sedimentary formations, characteristic scale values have been linked to lithological layering (Odling et al., 1999; Ackermann et al., 2001). Further measurements in lava flows may be required to evaluate the impact of the lava-flow thickness on the fracture length distribution, and assess whether processes controlling fracture length in volcanic rocks are comparable to those operating in layered sedimentary systems (Schöpfer et al., 2011). The chemical composition of the lava, and hence its viscosity and thermal conductivity, as well as the temperature and phase of the cooling fluid (air, water or ice), impact the cooling rate of the lava flow (Lore et al., 2001; Conway et al., 2015) and may thus also control the scaling of fracture length. The scale of the exponential distribution has also been reported to reflect a feedback process during fracture growth (Renshaw & Park, 1997). Field observations (Schaefer & Kattenhorn, 2004) and numerical models (Lore et al., 2000, 2001) have shown that neighbouring fractures develop a hierarchy of leading and trailing fractures, which interact with each other, and may cause such feedback process.

5.2. Column-forming Fracture Intensity

While the orientations and lengths of the column-forming fractures are well constrained from the 1-D and 2-D measurements, the fracture intensity in 3-D is less constrained. P_{21} and P_{32} fracture intensity parameters are traditionally measured from trace maps of the intersections between fractures and an outcrop face, i.e. the fracture edges, while TLS processing used here provides the location and geometry of fracture faces. The evaluation of P_{21} fracture intensity on the outcrop surface, although assumes that fractures are fully tessellated and share

19

edges, is preferred to the virtual section trace maps because it uses the TLS-processed fracture dimensions directly. As the two P_{21} measurement techniques provide similar results (Figure 11), we are confident that the resulting values are representative of the outcrop. P_{21} values are slightly under-estimated by the lack of detection of in-plane fractures (see Section 3.3).

The 2.4–$2.5 \, \text{m}^{-1}$ fracture intensity P_{32} values relate only to the steeply-dipping column-forming fractures, as gently-dipping fractures were not sampled by TLS processing. Gently-dipping fractures are fewer and shorter (rarely $>3 \, \text{m}$ long, as indicated by the manual scanline) than steeply-dipping ones, so the P_{32} for gently-dipping fractures is a small fraction of the P_{32} for steeply-dipping fractures. Therefore, the estimated $\sim 0.5 \, \%$ fracture porosity for the steeply-dipping column-forming fractures is supplemented by an additional small contribution from the gently-dipping column-forming and platy fractures.

5.3. Controls on the Geometry of Column-forming Fractures

An interpretive diagram of the fracture system geometry within the Happy Valley outcrop highlights the high connectivity of column-forming fractures, and the role of platy fractures and breccias on the fracture system (Figure 12). Column-forming fractures commonly terminate at, or curve parallel to, the platy fractures, forming blocks that are well connected to each other. Platy fractures thus have a strong impact on the organisation of the fracture system. Even where platy fractures are not fully open and detectable, they may control deflection or arrest of column-forming fractures. Similarly, layering such as flow-banding, and dilatant fractures parallel to the lava flow, may interact with, and result in the termination of, column-forming fractures perpendicular to the lower breccia (Schaefer & Kattenhorn, 2004).

Where observed, the column-forming fractures either stop, or bifurcate at the blocky-breccia interface. This configuration provides connections for flow pathways between the blocky and the breccia sections of the lava flow. Breccia clasts are fitted by fracture planes during the TLS processing. P_{10} fracture density values do not vary between the blocky and breccia facies (Figure 10a),

however, the breccia zone in the northern part of the outcrop has fewer large fractures ($>5\,\mathrm{m}$) than the blocky zone (Figure 9). This difference in fracture size is reflected in the P_{21} value which is higher in the breccia than in the blocky zone. P_{10} fracture intensity does not include the fracture size, and the P_{21} measure is preferred here as the intensity measure.

Fracture density and size vary locally within the Happy Valley outcrop, although these variations are not systematic up or along the exposure (Figure 10). Outcrop observations (DeGraff et al., 1989), supported by numerical models of fracture density in basalt lava flows (Lore et al., 2001), indicate that fracture density is typically higher near the margins than in the interior of the flow, due to the faster cooling rate closer to the margins. Similarly, observations from the Meads Wall dyke ($400\,\mathrm{m}$ from Happy Valley) and similar lava flows located on Ruapehu show that this higher density occurs within 0.1–$0.5\,\mathrm{m}$ of the cooling surfaces. This higher fracture density near the margins of breccias is not observed at Happy Valley, which may be due to the limited exposure of lava flow margins.

5.4. Comparison of results with previous studies

Previously published fracture geometry measurements on Ruapehu focused on ice-lava contacts (Spörli & Rowland, 2006; Conway et al., 2015). Overall, lavas of the Mangawhero and Whakapapa Formations which have been in contact with ice have similar column-forming fracture average length ($1\,\mathrm{m}$), and slightly higher P_{10} values (3–$10\,\mathrm{m}^{-1}$) than those measured at Happy Valley due to higher cooling rates (Conway et al., 2015, 2016). The small spacing and short length of platy fractures at Happy Valley is similar to that reported by Conway et al. (2015), but these fractures are less pervasive at Happy Valley than in lavas which cooled in contact with ice.

Fracture densities (P_{10}) at Happy Valley are slightly lower ($0.6\,\mathrm{m}^{-1}$) than those of the extensively studied Box Canyon basalt flows in the U.S.A./ (0.8-2.5 DeGraff & Aydin, 1987; Lore et al., 2000). Measurements at Happy Valley also match the lower bounds of relationships between (1) fracture length and lava

flow thickness of 10:1 (lava flow thickness of 820 m and median length of 1 m), and (2) mean length and lava SiO_2 content compiled by Hetényi et al. (2011) for numerous single-unit flows similar to Happy Valley. The ratio of column height to width, close to 1 at Happy Valley as seen by TLS measurements of fractures in vertical and horizontal directions, is similar to felsic flows generally having stouter columns than mafic flows, due to the cooling conditions controlled by different mechanical and thermal properties of the lavas (Hetényi et al., 2011).

5.5. Potential Effects of the Fracture System on Reservoir Permeability

The column-forming fractures observed in lava flow outcrops are at least partially retained during burial and further exhumation, as described in epithermal deposits hosted in andesite and rhyolite lavas in the Coromandel Peninsula, New Zealand (Brathwaite et al., 2001; Zuquim & Rowland, 2013). In these systems, some veins and hydrothermal breccias (that represent paleo-fluid flow pathways) formed along column-forming fractures and flow-banding, indicating that these structures can control permeability.

Breccias at Happy Valley are weak, heterogeneous, and of high matrix porosity. Therefore, breccias affect fracture propagation by forming a mechanical interface, and also have a high permeability potential. The resulting flow pathways in breccias may be better developed laterally, along the borders of the lava flow, than vertically, as these breccias have limited thickness. Such lateral flow pathways controlled by brecciated margins of buried rhyolitic lava flows are suggested at the Tauhara and Ohaaki geothermal fields, TVZ (Milloy & Lim, 2012; Mroczek et al., 2016). Connections between breccias of adjacent lava flows have the potential to further enhance lateral connectivity and permeability at the scale of several lava flows.

Conversely, permeability measurements in boreholes in the basaltic volcanic island of Mayotte (Comoros) indicated that most of the fluid flow occurs within a fractured lava flow interior rather than in the brecciated zone (Lachassagne et al., 2014). This suggests that in some cases, the low strength and cohesion of breccias make them more vulnerable than the blocky interior to erosion (while

on the surface), compaction, hydrothermal alteration, and other processes that could decrease permeability (Custodio, 2007). Hydrothermal alteration within the andesite-hosted Rotokawa Geothermal Field is generally more intense in the pseudo-breccias and breccias than the massive lavas, presumably due to greater fluid-rock interactions (Andersen, 2011) associated with rapid precipitation kinetics and high flow rates. Intense breccia alteration in reservoirs can decrease permeability in different ways: directly via mineral deposition, which decreases porosity and associated permeability (a relationship quantified for the Rotokawa geothermal field by Siratovich et al., 2014), or associated with the deformation of highly altered rocks which can result in a decrease of porosity (and hence permeability) even with a decreased strength (Siratovich et al., 2016). Even for weakly or moderately altered breccias, the higher tortuosity of flow pathways caused by the clasts may decrease permeability (Heap et al., 2014) compared to a network of planar column-forming fractures. The entire history of reservoir andesites, from emplacement at the surface to reservoir rock, thus influences permeability which can vary at short length scales, as demonstrated by variations of alteration intensity observed over tens of centimetres in cores (Massiot et al., 2015b) or measured in reservoir over a few hundred of metres (see discussion in Siratovich et al., 2016; Hernandez et al., 2015).

Similar to faults (Rowland & Simmons, 2012), breccias may thus also form conduits or barriers to fluid flow. Where breccias decrease permeability, they may compartmentalise reservoirs. Such compartmentalisation is observed in the Rotokawa reservoir (Hernandez et al., 2015), although it is not clear whether the compartmentalisation is related to faults (McNamara et al., 2015; Sherburn et al., 2015); the internal structure of the 1 km-thick series of lavas, pseudo-breccias and breccias; or a combination of both.

5.6. Fracture System Modelling for Happy Valley-type Lava Flows

Figure 13 presents DFN models of the blocky zone at Happy Valley based on three P_{33} values and the three length distributions considered in this paper (exponential, log-normal and power-law, even if the power-law distribution

23

does not fit the data well; all parameters are listed in Table 1). The DFNs are composed of two rectangular fracture sets: sub-vertical and sub-horizontal (Figure 13a). The input density value for each model is the P_{32} parameter; below, we discuss the effect of varying fracture density using the fracture porosity P_{33} using a mean aperture of 2 mm (equation 5). To illustrate differences between models, a virtual trace map dipping at 45° sampling both fracture sets displays fracture traces intersecting the plane in each model (Figure 13b). Two parameters are used to compare the fracture networks: the volume of fractures intersected by the plane, and the fracture volume connected to the trace map plane as a percentage of the entire fracture network. In a reservoir in which boreholes intersect fractures, the intersected fracture volume would correspond to the volume of fluids directly accessible, while the connected volume would correspond to the volume of fluids potentially recoverable.

Increasing P_{33} raises the volume of fractures intersected by the trace map, as well as the level of connectivity: nearly all (>97 vol. %) fractures are connected to the trace map at 0.53 % porosity and above, which is the P_{33} value estimated at Happy Valley (Figure 13b). The volume of fractures intersected by the trace map plane is smallest with a power-law length distribution for $P_{33} \geq 0.53$ %, and highest with an exponential length distribution. The length distribution also affects the level of connectivity, particularly for P_{33} of 0.14 % where the network is only partially connected.

A total P_{33} value of 0.53 %, together with the other geometrical parameters evaluated in this paper (Table 1), allows the fracture system to be almost completely connected (97.6 %; Figure 13b). While there is some uncertainty on the analysis of the three components of the P_{33} (namely the P_{21}, C_{32} and aperture), the fact that the numerical model provides a high level of connectivity similar to outcrop observations increases confidence in the reliability of the estimated parameters. With this level of connectivity, it is interesting to note that the choice of fracture length distribution does not significantly affect the percentage of connectivity; however, it does affect the volume of fractures connected to the trace map. This 'total' ~0.5 % fracture porosity may be considered low

24

compared to the matrix porosity (2–5 %), but the macro-fracture system of column-forming fractures is better connected and less tortuous than the micro-cracks and vesicles network governing matrix porosity, and hence likely exerts greater controls on the bulk permeability. Considerations of permeability k with a 3-D isotropic array of parallel fractures aligned with the flow, as would be the case for vertical flow at Happy Valley, using a parallel plate model, yield: $k = a^3/(S * 12)$ where S is the mean fracture spacing (inverse of P_{10}) and a the mean aperture (Phillips, 1991). This simple model yields a permeability on the order of $10^{-9}\,\mathrm{m}^2$ at Happy Valley, on the high range of bulk permeability in basalts (Brace, 1980) and four orders of magnitude higher than in an unnamed andesite-hosted geothermal system (Wallis et al., 2015).

The most uncertain parameter of these DFN models, though critical to model permeability, is the fracture transmissivity derived from fracture aperture. Here, we have used a normally distributed aperture with a mean of 2 mm. Measurements of length/aperture ratios on site-specific reservoir analogues may provide better estimations; Gudmundsson et al. (2001) reports a ∼400 ratio value measured on veins in basaltic rocks, whereas power-law relationships between fracture hydraulic aperture and length have also been used (Baghbanan & Jing, 2007). However, the fracture aperture actively contributing to the permeability depends on the roughness of the fracture planes (Ishibashi et al., 2014). Fracture roughness itself depends on the connected matrix porosity and the resulting tortuosity, as shown by Heap & Kennedy (2016) in experimental measurements for lava flows of the same formation as the Happy Valley outcrop. In addition, the *in-situ* stresses in a reservoir would control the fracture aperture, e.g. by closing those fractures with little asperities orthogonal to σ_1 (maximum principal stress; Barton et al., 2013) or keeping open those with a high slip tendency (Townend & Zoback, 2000). For reservoir modelling applications, geometrical fracture parameters evaluated in this work should be adapted to fit available reservoir data.

6. Conclusion

The Happy Valley lava flow studied represents a young, 5–20 m-thick lava flow of andesitic composition which flowed over a gently-dipping paleo-topography. The acquisition, processing and analysis of TLS point clouds outlined in this paper are suitable methods for quantifying fracture systems of blocky lava flows formed during their emplacement and cooling. The automatic Facets algorithm for extracting fracture planes permits a consistent processing of the dataset across a large outcrop, while requiring sufficient user input and calibration from other measurements to ensure its validity. The fracture system comprises column-forming fractures that produce the blocky part of the outcrop, flow-parallel clustered platy fractures which locally increase the fracture density and affect the propagation of column-forming fractures, and breccias at the margins of the lava flow. Column-forming fractures are oriented either sub-parallel or sub-perpendicular to the margins of the lave flow (i.e., subhorizontal or sub-vertical in this case), without mean strike orientation. The length of steeply-dipping column-forming fractures, which is well sampled by the TLS, is best approximated by a scale-dependent exponential distribution. The areal and volumetric fracture intensities reveal a well-connected system within the blocky region, partially connected to the breccias, with a ~0.5 % fracture porosity. This seemingly low fracture porosity has a significant impact on the permeability within the lava flow due to the high connectivity and planarity of column-forming fractures. High porosity breccias may have a varied influence on permeability in reservoirs, depending on the burial and hydrothermal alteration history; breccia have the potential to promote lateral flow pathways, or to form flow barriers. Discrete fracture network models generated from fracture geometries estimated from the TLS analysis and manual scanline measurements yield a highly connected network, in agreement with outcrop observations.

26

Acknowledgments

27

References

Abellan, A., Derron, M.-H., & Jaboyedoff, M. (2016). "Use of 3d point clouds in geohazards" special issue: Current challenges and future trends. *Remote Sensing*, *8*, 130. doi:10.3390/rs8020130.

Ackermann, R. V., Schlische, R. W., & Withjack, M. O. (2001). The geometric and statistical evolution of normal fault systems: an experimental study of the effects of mechanical layer thickness on scaling laws. *Journal of Structural Geology*, *23*, 1803–1819. doi:10.1016/s0191-8141(01)00028-1.

Aler, J., Mouza, J. D., & Arnould, M. (1996). Measurement of the fragmentation efficiency of rock mass blasting and its mining applications. *International Journal of Rock Mechanics and Mining Sciences & Geomechanics Abstracts*, *33*, 125–139. doi:10.1016/0148-9062(95)00054-2.

Andersen, L. (2011). *A comparison of buried andesites at Ngatamariki and Rotokawa geothermal fields, Taupo*. Msc The University of Waikato, New Zealand.

Arnórsson, S. (1995). Geothermal systems in Iceland: Structure and conceptual models—I. High-temperature areas. *Geothermics*, *24*, 561–602. doi:10.1016/0375-6505(95)00025-9.

Baghbanan, A., & Jing, L. (2007). Hydraulic properties of fractured rock masses with correlated fracture length and aperture. *International Journal of Rock Mechanics and Mining Sciences*, *44*, 704–719. doi:10.1016/j.ijrmms.2006.11.001.

Barton, C. A., Moos, D., Hartley, L., Baxter, S., Foulquier, L., Holl, H., & Hogarth, R. (2013). Geomechanically coupled simulation of flow in fractured reservoirs. *Proceedings of the 38th workshop on geothermal engineering, Stanford*, .

28

Barton, C. A., Zoback, M. D., & Moos, D. (1995). Fluid flow along potentially active faults in crystalline rock. *Geology*, *23*, 683–686. doi:10.1130/0091-7613(1995)023<0683:FFAPAF>2.3.CO;2.

Bemis, S. P., Micklethwaite, S., Turner, D., James, M. R., Akciz, S., Thiele, S. T., & Bangash, H. A. (2014). Ground-based and UAV-based photogrammetry: A multi-scale, high-resolution mapping tool for structural geology and paleoseismology. *Journal of Structural Geology*, *69*, 163–178. doi:10.1016/j.jsg.2014.10.007.

Berkowitz, B. (2002). Characterizing flow and transport in fractured geological media: A review. *Advances in Water Resources*, *25*, 861–884. doi:10.1016/s0309-1708(02)00042-8.

Bertani, R. (2016). Geothermal power generation in the world 2010–2014 update report. *Geothermics*, *60*, 31–43. doi:10.1016/j.geothermics.2015.11.003.

Bonnet, E., Bour, O., Odling, N. E., Davy, P., Main, I., Cowie, P., & Berkowitz, B. (2001). Scaling of fracture systems in geological media. *Reviews of Geophysics*, *39*, 347–383. doi:10.1029/1999rg000074.

Bonnichsen, B., & Kauffman, D. F. (1987). Physical features of rhyolite lava flows in the Snake River Plain volcanic province, southwestern Idaho. *Geological Society of America Special Papers*, *212*, 119–145.

Brace, W. (1980). Permeability of crystalline and argillaceous rocks. *International Journal of Rock Mechanics and Mining Sciences & Geomechanics Abstracts*, *17*, 241–251. doi:10.1016/0148-9062(80)90807-4.

Brathwaite, R. L., Cargill, H. J., Christie, A. B., & Swain, A. (2001). Lithological and spatial controls on the distribution of quartz veins in andesite- and rhyolite-hosted epithermal Au-Ag deposits of the Hauraki Goldfield, New Zealand. *Mineralium Deposita*, *36*, 1–12. doi:10.1007/s001260050282.

Buckley, S. J., Howell, J., Enge, H., & Kurz, T. (2008). Terrestrial laser scanning in geology: data acquisition, processing and accuracy considerations. *Journal of the Geological Society*, *165*, 625–638. doi:10.1144/0016-76492007-100.

Carbotte, S. M., & Macdonald, K. C. (1994). Comparison of seafloor tectonic fabric at intermediate, fast, and super fast spreading ridges: Influence of spreading rate, plate motions, and ridge segmentation on fault patterns. *Journal of Geophysical Research: Solid Earth*, *99*, 13609–13631. doi:10.1029/93jb02971.

Chen, R.-H., Lee, C.-H., & Chen, C.-S. (2001). Evaluation of transport of radioactive contaminant in fractured rock. *Environmental Geology*, *41*, 440–450. doi:10.1007/s002540100410.

CloudCompare (2016). version 2.6.2 (GPL software). http://cloudcompare.org. URL: http://www.cloudcompare.org.

Conway, C. E., Leonard, G. S., Townsend, D. B., Calvert, A. T., Wilson, C. J., Gamble, J. A., & Eaves, S. R. (2016). A high-resolution 40Ar/39Ar lava chronology and edifice construction history for Ruapehu volcano, New Zealand. *Journal of Volcanology and Geothermal Research*, . doi:10.1016/j.jvolgeores.2016.07.006.

Conway, C. E., Townsend, D. B., Leonard, G. S., Wilson, C. J. N., Calvert, A. T., & Gamble, J. A. (2015). Lava-ice interaction on a large composite volcano: a case study from Ruapehu, New Zealand. *Bulletin of Volcanology*, *77*. doi:10.1007/s00445-015-0906-2.

Cruden, D. (1977). Describing the size of discontinuities. *International Journal of Rock Mechanics and Mining Sciences & Geomechanics Abstracts*, *14*, 133–137. doi:10.1016/0148-9062(77)90004-3.

Custodio, E. (2007). Groundwater in volcanic hard rocks. *Groundwater in fractured rocks: IAH Selected Paper Series*, *9*, 95–108.

DeGraff, J. M., & Aydin, A. (1987). Surface morphology of columnar joints and its significance to mechanics and direction of joint growth. *Geological Society of America Bulletin*, *99*, 605–617. doi:`10.1130/0016-7606(1987)99<605:SMOCJA>2.0.CO;2`.

DeGraff, J. M., & Aydin, A. (1993). Effect of thermal regime on growth increment and spacing of contraction joints in basaltic lava. *Journal of Geophysical Research: Solid Earth*, *98*, 6411–6430. doi:`10.1029/92jb01709`.

DeGraff, J. M., Long, P. E., & Aydin, A. (1989). Use of joint-growth directions and rock textures to infer thermal regimes during solidification of basaltic lava flows. *Journal of Volcanology and Geothermal Research*, *38*, 309–324. doi:`10.1016/0377-0273(89)90045-0`.

Deng, B.-w., Lee, C.-h., & Chang, J.-l. (1995). Characterization and interpretation of variability of fracture pattern in jointed andesites, Lan-Yu, Taiwan. *Journal of the Chinese Institute of Engineers*, *18*, 787–799. doi:`10.1080/02533839.1995.9677747`.

Deparis, J., Fricout, B., Jongmans, D., Villemin, T., Effendiantz, L., & Mathy, A. (2008). Combined use of geophysical methods and remote techniques for characterizing the fracture network of a potentially unstable cliff site (the 'Roche du Midi', Vercors massif, France). *Journal of Geophysics and Engineering*, *5*, 147–157. doi:`10.1088/1742-2132/5/2/002`.

Dershowitz, W. S., & Einstein, H. H. (1988). Characterizing rock joint geometry with joint system models. *Rock Mechanics and Rock Engineering*, *21*, 1988. doi:`10.1007/BF01019674`.

Dershowitz, W. S., & Herda, A. H. (1992). Interpretation of fracture spacing and intensity. *33th U.S. Symposium on Rock Mechanics (USRMS)*, .

Dewez, T. B., Girardeau-Montaut, D., Allanic, C., & Rohmer, J. (2016). FACETS: a Cloudcompare plugin to extract geological planes from unstruc-

tured 3D point clouds. *Int. Arch. Photogramm. Remote Sens. Spatial Inf. Sci.*, *XLI-B5*, 799–804. doi:10.5194/isprsarchives-xli-b5-799-2016.

Doyuran, V., Ayday, C., & Karahanoglu, N. (1993). Statistical analyses of discontinuity parameters of Gölbaši (Ankara) Andesites, Süpren (Eskišehir) marble, and Porsuk Dam (Eskišehir) peridotite in Turkey. *Bulletin of the International Association of Engineering Geology*, *48*, 15–31. doi:10.1007/bf02594973.

de Dreuzy, J.-R., Pichot, G., Poirriez, B., & Erhel, J. (2013). Synthetic benchmark for modeling flow in 3D fractured media. *Computers & Geosciences*, *50*, 59–71. doi:10.1016/j.cageo.2012.07.025.

Enge, H. D., Buckley, S. J., Rotevatn, A., & Howell, J. A. (2007). From outcrop to reservoir simulation model: Workflow and procedures. *Geosphere*, *3*, 469–490. doi:10.1130/ges00099.1.

Fabuel-Perez, I., Hodgetts, D., & Redfern, J. (2010). Integration of digital outcrop models (DOMs) and high resolution sedimentology - workflow and implications for geological modelling: Oukaimeden Sandstone Formation, High Atlas (Morocco). *Petroleum Geoscience*, *16*, 133–154. doi:10.1144/1354-079309-820.

Feng, Z.-Q. (2008). Volcanic rocks as prolific gas reservoir: A case study from the Qingshen gas field in the Songliao Basin, NE China. *Marine and Petroleum Geology*, *25*, 416–432. doi:10.1016/j.marpetgeo.2008.01.008.

Ferrero, A. M., Forlani, G., Roncella, R., & Voyat, H. I. (2009). Advanced Geostructural Survey Methods Applied to Rock Mass Characterization. *Rock Mechanics and Rock Engineering*, *42*, 631–665. doi:10.1007/s00603-008-0010-4.

Forbes, A., Blake, S., Tuffen, H., & Wilson, A. (2014). Fractures in a trachyandesitic lava at Öræfajökull, Iceland, used to infer subglacial emplacement

in 1727–8 eruption. *Journal of Volcanology and Geothermal Research*, *288*, 8–18. doi:10.1016/j.jvolgeores.2014.10.004.

Fournier, R. (1998). Hydrothermal Processes Related to Movement of Fluid From Plastic into Brittle Rock in the Magmatic-Epithermal Environment. *Economic Geology*, *94*, 1193–1211. doi:10.2113/gsecongeo.94.8.1193.

Gamble, J. A., Price, R. C., Smith, I. E. M., Mcintosh, W. C., & Dunbar, N. W. (2003). 40Ar/39Ar geochronology of magmatic activity, magma flux and hazards at Ruapehu volcano, Taupo Volcanic Zone, New Zealand. *Journal of Volcanology and Geothermal Research*, *120*, 271–287. doi:10.1016/S0377-0273(02)00407-9.

García-Sellés, D., Falivene, O., Arbués, P., Gratacos, O., Tavani, S., & Muñoz, J. (2011). Supervised identification and reconstruction of near-planar geological surfaces from terrestrial laser scanning. *Computers & Geosciences*, *37*, 1584–1594. doi:10.1016/j.cageo.2011.03.007.

García-Sellés, D., Gratacós, O., Muñoz, J., & Sarmiento, S. (2016). Characterization of geological structures with technical improvements in acquisition and processing. *Proceedings of the 2nd Virtual Geoscience Conference, Bergen, Norway, 21-23 September 2016*, (pp. 76–77).

Geyer, A., García-Sellés, D., Pedrazzi, D., Barde-Cabusson, S., Marti, J., & Muñoz, J. (2015). Studying monogenetic volcanoes with a terrestrial laser scanner: case study at Croscat volcano (Garrotxa Volcanic Field, Spain). *Bulletin of Volcanology*, *77*. doi:10.1007/s00445-015-0909-z.

Gigapan (2016). Gigapan. http://www.gigapan.com. URL: http://www.gigapan.com.

Gigli, G., & Casagli, N. (2011). Semi-automatic extraction of rock mass structural data from high resolution LIDAR point clouds. *International Journal of Rock Mechanics and Mining Sciences*, *48*, 187–198. doi:10.1016/j.ijrmms.2010.11.009.

33

Grossenbacher, K. A., & McDuffie, S. M. (1995). Conductive cooling of lava: columnar joint diameter and stria width as functions of cooling rate and thermal gradient. *Journal of Volcanology and Geothermal Research*, *69*, 95–103. doi:10.1016/0377-0273(95)00032-1.

Gudmundsson, A., Berg, S. S., Lyslo, K. B., & Skurtveit, E. (2001). Fracture networks and fluid transport in active fault zones. *Journal of Structural Geology*, *23*, 343–353. doi:10.1016/s0191-8141(00)00100-0.

Hackett, W. R., & Houghton, B. F. (1989). A facies model for a quaternary andesitic composite volcano: Ruapehu, New Zealand. *Bulletin of Volcanology*, *51*, 51–68. doi:10.1007/bf01086761.

Hardebol, N., & Bertotti, G. (2013). DigiFract: A software and data model implementation for flexible acquisition and processing of fracture data from outcrops. *Computers & Geosciences*, *54*, 326–336. doi:10.1016/j.cageo.2012.10.021.

Heap, M., Lavallée, Y., Petrakova, L., Baud, P., Reuschle, T., Varley, N., & Dingwell, D. B. (2014). Microstructural controls on the physical and mechanical properties of edifice-forming andesites at Volcán de Colima, Mexico. *Journal of Geophysical Research: Solid Earth*, *119*, 2925–2963. doi:10.1002/2013JB010521.

Heap, M. J., & Kennedy, B. M. (2016). Exploring the scale-dependent permeability of fractured andesite. *Earth and Planetary Science Letters*, *447*, 139–150. doi:10.1016/j.epsl.2016.05.004.

Hernandez, D., Clearwater, J., Burnell, J., Franz, P., Azwar, L., & Marsh, A. (2015). Update on the Modeling of the Rotokawa Geothermal System: 2010-2014. *Proceedings of the World Geothermal Congress*, .

Hetényi, G., Taisne, B., Garel, F., Médard, É., Bosshard, S., & Mattsson, H. B. (2011). Scales of columnar jointing in igneous rocks: field measurements

and controlling factors. *Bulletin of Volcanology*, *74*, 457–482. doi:`10.1007/s00445-011-0534-4`.

Hodgetts, D. (2013). Laser scanning and digital outcrop geology in the petroleum industry: A review. *Marine and Petroleum Geology*, *46*, 335–354. doi:`10.1016/j.marpetgeo.2013.02.014`.

Hudson, J., & Priest, S. (1979). Discontinuities and rock mass geometry. *International Journal of Rock Mechanics and Mining Sciences & Geomechanics Abstracts*, *16*, 339–362. doi:`10.1016/0148-9062(79)90001-9`.

Ishibashi, T., Watanabe, N., Hirano, N., Okamoto, A., & Tsuchiya, N. (2014). Beyond-laboratory-scale prediction for channeling flows through subsurface rock fractures with heterogeneous aperture distributions revealed by laboratory evaluation. *Journal of Geophysical Research: Solid Earth*, *120*, 106–124. doi:`10.1002/2014JB011555`.

James, M. R., & Robson, S. (2012). Straightforward reconstruction of 3D surfaces and topography with a camera: Accuracy and geoscience application. *Journal of Geophysical Research: Earth Surface*, *117*. doi:`10.1029/2011JF002289`.

Jones, R. R., Mccaffrey, K. J. W., Imber, J., Wightman, R., Smith, S. A. F., Holdsworth, R. E., Clegg, P., Paola, N. D., Healy, D., & Wilson, R. W. (2008). Calibration and validation of reservoir models: the importance of high resolution, quantitative outcrop analogues. *Geological Society, London, Special Publications*, *309*, 87–98. doi:`10.1144/sp309.7`.

Karpuz, C., & Paşamehmetoğlu, A. (1997). Field characterisation of weathered Ankara andesites. *Engineering Geology*, *46*, 1–17. doi:`10.1016/s0013-7952(96)00002-6`.

Kattenhorn, S. A., & Schaefer, C. J. (2008). Thermal-mechanical modeling of cooling history and fracture development in inflationary basalt lava

flows. *Journal of Volcanology and Geothermal Research*, *170*, 181–197. doi:10.1016/j.jvolgeores.2007.10.002.

Kulatilake, P., Wathugala, D., & Stephansson, O. (1993). Joint network modelling with a validation exercise in Stripa mine, Sweden. *International Journal of Rock Mechanics and Mining Sciences & Geomechanics Abstracts*, *30*, 503–526. doi:10.1016/0148-9062(93)92217-e.

Lachassagne, P., Aunay, B., Frissant, N., Guilbert, M., & Malard, A. (2014). High-resolution conceptual hydrogeological model of complex basaltic volcanic islands: a Mayotte, Comoros, case study. *Terra Nova*, *26*, 307–321. doi:10.1111/ter.12102.

Lato, M. J., Diederichs, M. S., & Hutchinson, D. J. (2010). Bias Correction for View-limited Lidar Scanning of Rock Outcrops for Structural Characterization. *Rock Mechanics and Rock Engineering*, *43*, 615–628. doi:10.1007/s00603-010-0086-5.

Laubach, S. E., Olson, J. E., & Gross, M. R. (2009). Mechanical and fracture stratigraphy. *AAPG Bulletin*, *93*, 1413–1426. doi:10.1306/07270909094.

Lee, C.-C., Lee, C.-H., Yeh, H.-F., & Lin, H.-I. (2010). Modeling spatial fracture intensity as a control on flow in fractured rock. *Environmental Earth Sciences*, *63*, 1199–1211. doi:10.1007/s12665-010-0794-x.

Lescinsky, T., & Fink, H. (2000). Lava and ice interaction at stratovolcanoes: Use of characteristic features to determine past glacial extents and future volcanic hazards. *Journal of Geophysical Research: Solid Earth*, *105*, 23711–23726. doi:10.1029/2000JB900214.

Lore, J., Aydin, A., & Goodson, K. (2001). A deterministic methodology for prediction of fracture distribution in basaltic multiflows. *Journal of Geophysical Research: Solid Earth*, *106*, 6447–6459. doi:10.1029/2000JB900407.

Lore, J., Gao, H., & Aydin, A. (2000). Viscoelastic thermal stress in cooling basalt flows. *Journal of Geophysical Research: Solid Earth*, *105*, 23695–23709. doi:10.1029/2000JB900226.

Massey, C. I., Manville, V., Hancox, G. H., Keys, H. J., Lawrence, C., & McSaveney, M. (2010). Out-burst flood (lahar) triggered by retrogressive landsliding, 18 March 2007 at Mt Ruapehu, New Zealand—a successful early warning. *Landslides*, *7*, 303–315. doi:10.1007/s10346-009-0180-5.

Massiot, C., McNamara, D., & Lewis, B. (2015a). Processing and analysis of high temperature geothermal acoustic borehole image logs in the Taupo Volcanic Zone, New Zealand. *Geothermics*, *53*, 190–201. doi:10.1016/j.geothermics.2014.05.010.

Massiot, C., McNamara, D. D., Nicol, A., & Townend, J. (2015b). Fracture Width and Spacing Distributions from Borehole Televiewer Logs and Cores in the Rotokawa Geothermal Field, New Zealand. *World Geothermal Congress*, .

Mauldon, M., Dunne, W., & Rohrbaugh, M. (2001). Circular scanlines and circular windows: new tools for characterizing the geometry of fracture traces. *Journal of Structural Geology*, *23*, 247–258. doi:10.1016/s0191-8141(00)00094-8.

McCaffrey, K. J. W., Sleight, J. M., Pugliese, S., & Holdsworth, R. E. (2003). Fracture formation and evolution in crystalline rocks: Insights from attribute analysis. *Geological Society, London, Special Publications*, *214*, 109–124. doi:10.1144/gsl.sp.2003.214.01.07.

McNamara, D. D., Massiot, C., Lewis, B., & Wallis, I. C. (2015). Heterogeneity of structure and stress in the Rotokawa Geothermal Field, New Zealand. *Journal of Geophysical Research: Solid Earth*, *120*, 1243–1262. doi:10.1002/2014JB011480.

Milloy, S. F., & Lim, Y. W. (2012). Wairakei-Tauhara pressure regime update. *Proceedings of the New Zealand Geothermal Workshop*, .

Mroczek, E. K., Milicich, S. D., Bixley, P. F., Sepulveda, F., Bertrand, E. A., Soengkono, S., & Rae, A. J. (2016). Ohaaki geothermal system: Refinement of a conceptual reservoir model. *Geothermics*, *59*, 311–324. doi:`10.1016/j.geothermics.2015.09.002`.

Nelson, C. E., Hobbs, R. W., & Rusch, R. (2015). On the Use of Fractal Surfaces to Understand Seismic Wave Propagation in Layered Basalt Sequences. *Pure and Applied Geophysics*, *172*, 1879–1892. doi:`10.1007/s00024-014-0986-5`.

Nelson, C. E., Jerram, D. A., Hobbs, R. W., Terrington, R., & Kessler, H. (2011). Reconstructing flood basalt lava flows in three dimensions using terrestrial laser scanning. *Geosphere*, *7*, 87–96. doi:`10.1130/ges00582.1`.

Nemčok, M., Moore, J. N., Allis, R., & McCulloch, J. (2004). Fracture development within a stratovolcano: the Karaha-Telaga Bodas geothermal field, Java volcanic arc. *Geological Society, London, Special Publications*, *231*, 223–242. doi:`10.1144/gsl.sp.2004.231.01.13`.

Nemčok, M., Moore, J. N., Christensen, C., Allis, R., Powell, T., Murray, B., & Nash, G. (2007). Controls on the Karaha–Telaga Bodas geothermal reservoir, Indonesia. *Geothermics*, *36*, 9–46. doi:`10.1016/j.geothermics.2006.09.005`.

Odling, N. E., Gillespie, P., Bourgine, B., Castaing, C., Chiles, J. P., Christensen, N. P., Fillion, E., Genter, A., Olsen, C., Thrane, L., Trice, R., Aarseth, E., Walsh, J. J., & Watterson, J. (1999). Variations in fracture system geometry and their implications for fluid flow in fractures hydrocarbon reservoirs. *Petroleum Geoscience*, *5*, 373–384. doi:`10.1144/petgeo.5.4.373`.

Olariu, M. I., Ferguson, J. F., Aiken, C. L., & Xu, X. (2008). Outcrop fracture characterization using terrestrial laser scanners: Deep-water Jackfork

sandstone at Big Rock Quarry, Arkansas. *Geosphere*, *4*, 247. doi:10.1130/ges00139.1.

Pearce, M. A., Jones, R. R., Smith, S. A. F., & McCaffrey, K. J. W. (2011). Quantification of fold curvature and fracturing using terrestrial laser scanning. *AAPG Bulletin*, *95*, 771–794. doi:10.1306/11051010026.

Pfeifer, N., & Briese, C. (2007). Laser scanning - principles and applications. *3rd International Exhibition & Scientific Congress on Geodesy, Mapping, Geology, Geophysics, Novosibirsk, Russia*, .

Phillips, O. M. (1991). *Flow and reactions in permeable rocks*. Cambridge University Press.

Pickering, G., Bull, J., & Sanderson, D. (1995). Sampling power-law distributions. *Tectonophysics*, *248*, 1–20. doi:10.1016/0040-1951(95)00030-q.

Pollard, D., & Aydin, A. (1988). Progress in understanding jointing over the past century. *Geological Society of America Bulletin*, *100*, 1181–1204. doi:10.1130/0016-7606(1988)100<1181:PIUJOT>2.3.CO;2.

Pollyea, R. M., & Fairley, J. P. (2011). Estimating surface roughness of terrestrial laser scan data using orthogonal distance regression. *Geology*, *39*, 623–626. doi:10.1130/g32078.1.

Pollyea, R. M., & Fairley, J. P. (2012). Implications of spatial reservoir uncertainty for CO_2 sequestration in the east Snake River Plain, Idaho (USA). *Hydrogeology Journal*, *20*, 689–699. doi:10.1007/s10040-012-0847-1.

Pollyea, R. M., Fairley, J. P., Podgorney, R. K., & Mcling, T. L. (2014). Physical constraints on geologic CO_2 sequestration in low-volume basalt formations. *Geological Society of America Bulletin*, *126*, 344–351. doi:10.1130/b30874.1.

Price, R. C., Gamble, J. A., Smith, I. E. M., Maas, R., Waight, T., Stewart, R. B., & Woodhead, J. (2012). The Anatomy of an Andesite Volcano: a Time-Stratigraphic Study of Andesite Petrogenesis and Crustal Evolution

at Ruapehu Volcano, New Zealand. *Journal of Petrology*, *53*, 2139–2189. doi:10.1093/petrology/egs050.

Priest, S., & Hudson, J. (1981). Estimation of discontinuity spacing and trace length using scanline surveys. *International Journal of Rock Mechanics and Mining Sciences & Geomechanics Abstracts*, *18*, 183–197. doi:10.1016/0148-9062(81)90973-6.

Priest, S. D. (1993). *Discontinuity Analysis for Rock Engineering*. Springer Netherlands. URL: http://dx.doi.org/10.1007/978-94-011-1498-1. doi:10.1007/978-94-011-1498-1.

Priest, S. D. (2004). Determination of Discontinuity Size Distributions from Scanline Data. *Rock Mechanics and Rock Engineering*, *37*, 347–368. doi:10.1007/s00603-004-0035-2.

Renshaw, C., & Park, J. (1997). Effect of mechanical interactions on the scaling of fracture length and aperture. *Nature*, *386*, 482–484. doi:10.1038/386482a0.

Riegl (2010). Riegl. http://www.riegl.com/uploads/tx_pxpriegldownloads/10_DataSheet_Z420i_03-05-2010.pdf. URL: http://www.riegl.com/uploads/tx_pxpriegldownloads/10_DataSheet_Z420i_03-05-2010.pdf.

Riquelme, A. J., Abellán, A., Tomás, R., & Jaboyedoff, M. (2014). A new approach for semi-automatic rock mass joints recognition from 3D point clouds. *Computers & Geosciences*, *68*, 38–52. doi:10.1016/j.cageo.2014.03.014.

Rotevatn, A., Buckley, S. J., Howell, J. A., & Fossen, H. (2009). Overlapping faults and their effect on fluid flow in different reservoir types: A LIDAR-based outcrop modeling and flow simulation study. *AAPG Bulletin*, *93*, 407–427. doi:10.1306/09300807092.

Rowland, J. V., & Simmons, S. F. (2012). Hydrologic, Magmatic, and Tectonic Controls on Hydrothermal Flow, Taupo Volcanic Zone, New Zealand: Impli-

cations for the Formation of Epithermal Vein Deposits. *Economic Geology*, *107*, 427–457. doi:`10.2113/econgeo.107.3.427`.

Sari, M., Karpuz, C., & Ayday, C. (2010). Estimating rock mass properties using Monte Carlo simulation: Ankara andesites. *Computers & Geosciences*, *36*, 959–969. doi:`10.1016/j.cageo.2010.02.001`.

Schaefer, C. J., & Kattenhorn, S. A. (2004). Characterization and evolution of fractures in low-volume pahoehoe lava flows, eastern Snake River Plain, Idaho. *Geological Society of America Bulletin*, *116*, 322–336. doi:`10.1130/b25335.1`.

Schnabel, R., Wahl, R., & Klein, R. (2007). Efficient RANSAC for Point-Cloud Shape Detection. *Computer Graphics Forum*, *26*, 214–226. doi:`10.1111/j.1467-8659.2007.01016.x`.

Schöpfer, M. P., Arslan, A., Walsh, J. J., & Childs, C. (2011). Reconciliation of contrasting theories for fracture spacing in layered rocks. *Journal of Structural Geology*, *33*, 551–565. doi:`10.1016/j.jsg.2011.01.008`.

Sherburn, S., Sewell, S., Bourguignon, S., Cumming, W., Bannister, S., Bardsley, C., Winick, J., Quinao, J., & Wallis, I. (2015). Microseismicity at Rotokawa geothermal field, New Zealand, 2008–2012. *Geothermics*, *54*, 23–34. doi:`10.1016/j.geothermics.2014.11.001`.

Siratovich, P. A., Heap, M. J., Villeneuve, M. C., Cole, J. W., Kennedy, B. M., Davidson, J., & Reuschlé, T. (2016). Mechanical behaviour of the Rotokawa Andesites (New Zealand): Insight into permeability evolution and stress-induced behaviour in an actively utilised geothermal reservoir. *Geothermics*, *64*, 163–179. doi:`10.1016/j.geothermics.2016.05.005`.

Siratovich, P. A., Heap, M. J., Villeneuve, M. C., Cole, J. W., & Reuschlé, T. (2014). Physical property relationships of the Rotokawa Andesite, a significant geothermal reservoir rock in the Taupo Volcanic Zone, New Zealand. *Geothermal Energy*, *2*. doi:`10.1186/s40517-014-0010-4`.

41

Spörli, K., & Rowland, J. (2006). 'Column on column' structures as indicators of lava/ice interaction, Ruapehu andesite volcano, New Zealand. *Journal of Volcanology and Geothermal Research*, *157*, 294–310. doi:`10.1016/j.jvolgeores.2006.04.004`.

Sturzenegger, M., & Stead, D. (2009a). Close-range terrestrial digital photogrammetry and terrestrial laser scanning for discontinuity characterization on rock cuts. *Engineering Geology*, *106*, 163–182. doi:`10.1016/j.enggeo.2009.03.004`.

Sturzenegger, M., & Stead, D. (2009b). Quantifying discontinuity orientation and persistence on high mountain rock slopes and large landslides using terrestrial remote sensing techniques. *Natural Hazards and Earth System Sciences*, *9*, 267–287. doi:`10.5194/nhess-9-267-2009`.

Terzaghi, R. D. (1965). Sources of Error in Joint Surveys. *Géotechnique*, *15*, 287–304. doi:`10.1680/geot.1965.15.3.287`.

Tost, M., & Cronin, S. J. (2015). Linking distal volcaniclastic sedimentation and stratigraphy with the development of Ruapehu volcano, New Zealand. *Bulletin of Volcanology*, *77*. doi:`10.1007/s00445-015-0977-0`.

Townend, J., & Zoback, M. D. (2000). How faulting keeps the crust strong. *Geology*, *28*, 399–402. doi:`10.1130/0091-7613(2000)28<399:HFKTCS>2.0.CO;2`.

Umili, G., Ferrero, A., & Einstein, H. (2013). A new method for automatic discontinuity traces sampling on rock mass 3D model. *Computers & Geosciences*, *51*, 182–192. doi:`10.1016/j.cageo.2012.07.026`.

Vye-Brown, C., Self, S., & Barry, T. L. (2013). Architecture and emplacement of flood basalt flow fields: case studies from the Columbia River Basalt Group, NW USA. *Bulletin of Volcanology*, *75*. doi:`10.1007/s00445-013-0697-2`.

Wallis, I., Moon, H., Clearwater, J., Azwar, L., & Barnes, M. (2015). Perspectives on geothermal permeability. *Proceedings 37th New Zealand Geothermal Workshop*, .

Wang, X. (2005). *Stereological interpretation of rock fracture traces on borehole walls and other cylindrical surfaces*. Ph.d. Virginia Polytechnic Institute and State University. URL: `http://scholar.lib.vt.edu/theses/available/etd-09262005-164731/`.

Wilson, C., Houghton, B., McWilliams, M., Lanphere, M., Weaver, S., & Briggs, R. (1995). Volcanic and structural evolution of Taupo Volcanic Zone, New Zealand: a review. *Journal of Volcanology and Geothermal Research*, *68*, 1–28. doi:`10.1016/0377-0273(95)00006-g`.

Wilson, C. E., Aydin, A., Karimi-Fard, M., Durlofsky, L. J., Sagy, A., Brodsky, E. E., Kreylos, O., & Kellogg, L. H. (2011). From outcrop to flow simulation: Constructing discrete fracture models from a LIDAR survey. *AAPG Bulletin*, *95*, 1883–1905. doi:`10.1306/03241108148`.

Wysoczanski, R. (1989). *Volcanology and pretology of the Iwikau member, Whakapapa Formation, Mt Ruapehu, Tongariro Volcanic Centre, New Zealand*. B.sc. (Hns) Victoria University of Wellington, New Zealand.

Zhang, L., Einstein, H. H., & Dershowitz, W. S. (2002). Stereological relationship between trace length and size distribution of elliptical discontinuities. *Géotechnique*, *52*, 419–433. doi:`10.1680/geot.2002.52.6.419`.

Zuquim, M., & Rowland, J. V. (2013). Structural controls on fluid flow at the Onemana area, Coromandel Peninsula, New Zealand. *Proceedings of the 35th NZ Geothermal Workshop*, .
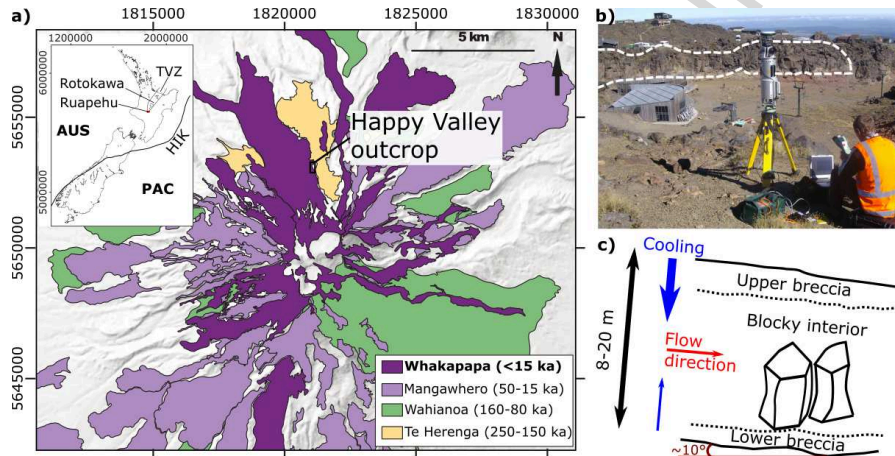
Figures

Figure 1: Location of the "Happy Valley" lava flow outcrop. a) Simplified geological map of Ruapehu Volcano with major formation distribution and ages (after Conway et al., 2016). The Happy Valley outcrop is shown by the black box. Locations of Ruapehu volcano at the southern tip of the Taupo Volcanic Zone (TVZ) is shown by the inset figure. The Hikurangi Trough (HIK) marks the seafloor expression of westward subduction of the Pacific plate (PAC) beneath the Australian plate (AUS). Extent of the geologic map of Ruapehu is shown by the red dot on inset map; NZTM2000 coordinate system. b) TLS acquisition; the outcrop studied is delimited by the dashed line. c) Schematic cross-section of the outcrop, a 8–20 m-thick blocky lava flow emplaced over a gently dipping paleo-slope ($\sim 10^{\circ}$). The upper and lower breccias displayed here are observable only in parts of the outcrop.

44
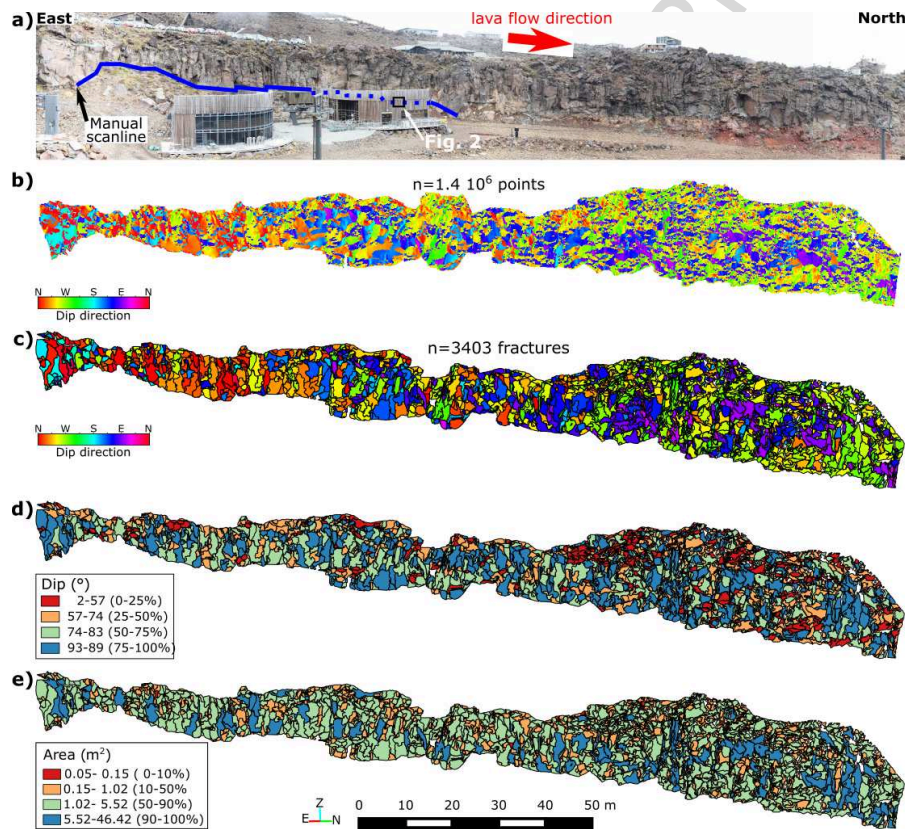
Figure 2: Fracture delineation of the Happy Valley terrestrial laser scanner (TLS) point cloud. a) Gigapan panoramic photograph composed of 430 individual photographs with the trace of the manual scanline (solid/dashed blue line) and the lava flow direction. b) TLS point cloud used for the fracture delineation and resampled every 4 cm, coloured by the local dip direction. c) Fractures delineated using the Facets plugin, coloured by dip direction, d) dip magnitude, and e) area. Note the non-regular ranges for the dip magnitude and area scales; the percentage of fractures falling into each category is indicated in brackets. *c-e: 3-D fractures projected onto a NW-SE striking, vertical plane. Each colour patch represents a single fracture.*
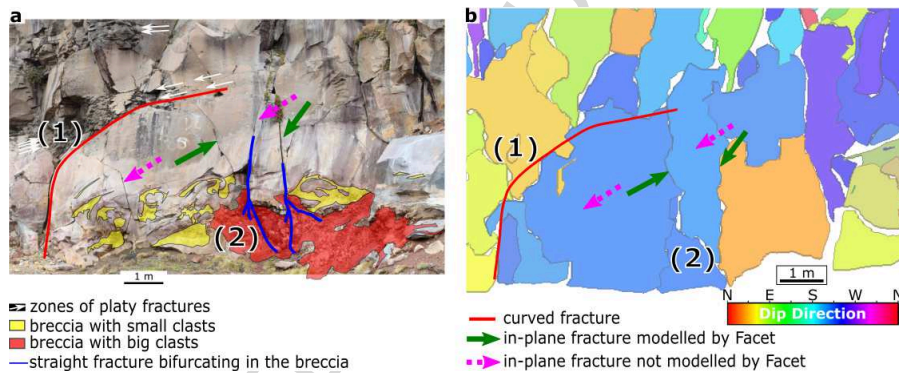
Figure 3: Detection limits of the TLS and factors influencing the column-forming fracture propagation. a) Section of the panoramic photograph displayed in Figure 2a. b) Fracture planes processed from the TLS point cloud with the Facets algorithm. Note the fitting of a single plane for the area of dense platy fractures (1); the absence of detection of breccia in the TLS (2); the limited detection of in-plane column-forming fractures (purple dotted arrows) (3); the bifurcations of fractures at the interface between the blocky interior and the brecciated zones (blue lines) and (4); the fitting of a platy fracture cluster (white arrows) by a single plane. The area is located behind the northern building (see Figure 2a). *A high-resolution version of the entire photograph presented in a) is available at: `http://www.gigapan.com/gigapans/191973`*.
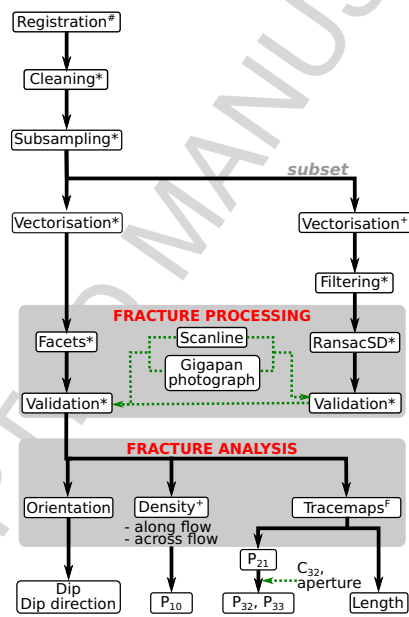
Figure 4: Flowchart of the TLS data processing and fracture analysis using a combination of Riegl RiscanPro (#), SEFL (+), CloudCompare v2.7.0 (*) with the RansacSD (Schnabel et al., 2007) and Facets plugin (Dewez et al., 2016), and Fracman (^{F}) software. Note that P_{ij} refers to the dimensionality of the sampling region (i) and the dimensionality of the fracture property (j).
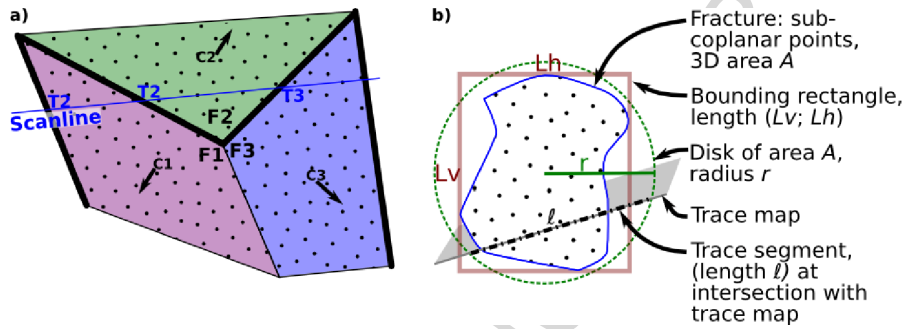
Figure 5: Fracture measurements on scanline, TLS-processed fractures, and trace maps. a) Schematic of the fracture sampling of three fractures (F1, F2 and F3): the scanline measures fractures at the intersection between the scanline and the fracture (T1, T2 and T3) while the TLS processing extracts the centre (C1, C2 and C3) of each fracture, the orientation (characterised by the normal to planes, arrows) and the size (3-D area A, lengths Lh and Lv). b) The bounding rectangle of the point subset of each fracture has length Lh and Lv in horizontal and vertical directions. The trace length ℓ is measured at the intersection between the trace map and the disk of radius r and area A.
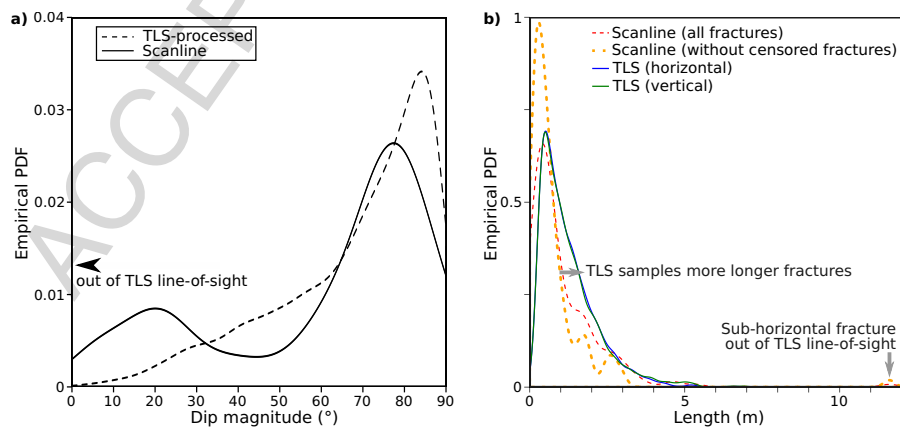

Figure 6: a) Empirical probability density function (PDF) of the dip magnitude for the scanline (corrected for Terzaghi sampling bias) and TLS-processed datasets. b) Empirical PDF of fracture length for the scanline (with and without censored fractures) and TLS-processed fractures (measured in horizontal and vertical directions).
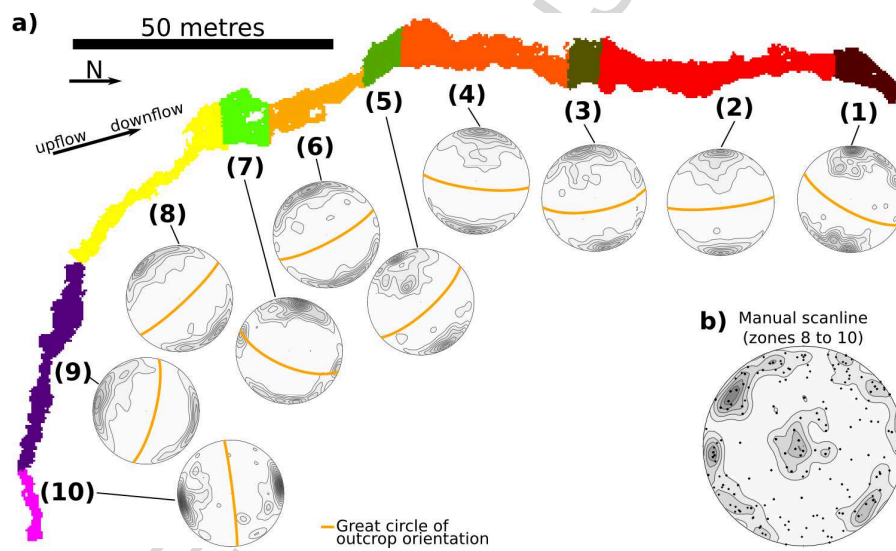
48

Figure 7: Orientation of column-forming fractures in relation to outcrop orientation. a) Plan view of the outcrop subdivided into 10 zones of constant orientation, accompanied by a stereonet of TLS-processed fracture orientations, and approximative lava flow direction. The outcrop orientation is plotted on each stereonet as a great circle. b) Stereonet with poles to planes sampled on the manual scanline (corrected for the Terzaghi orientation sampling bias). *All stereonets are Schmidt lower hemisphere projections, with Fisher density contouring spacing of 1%.*
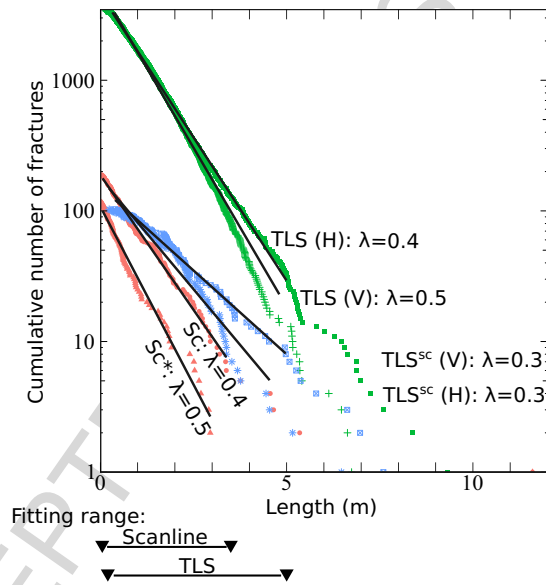
Figure 8: Complementary cumulative distribution function (CCDF) of fracture length in log-linear (semi-log) scale for fractures measured on the manual scanline (with (Sc) and without censored fractures ($Sc*$), orange symbols) and processed from the TLS (over the entire outcrop (TLS; green symbols) and in the manual scanline area (TLS^{sc}; blue symbols)) measured in sub-vertical (V) and sub-horizontal (H) orientations. Coefficients λ of the linear trends within truncation limits provides the exponential distribution parameter. All adjusted correlation coefficients are > 0.98, except the horizontal TLS-processed dataset in the scanline area (TLS^{sc}) which is 0.94.
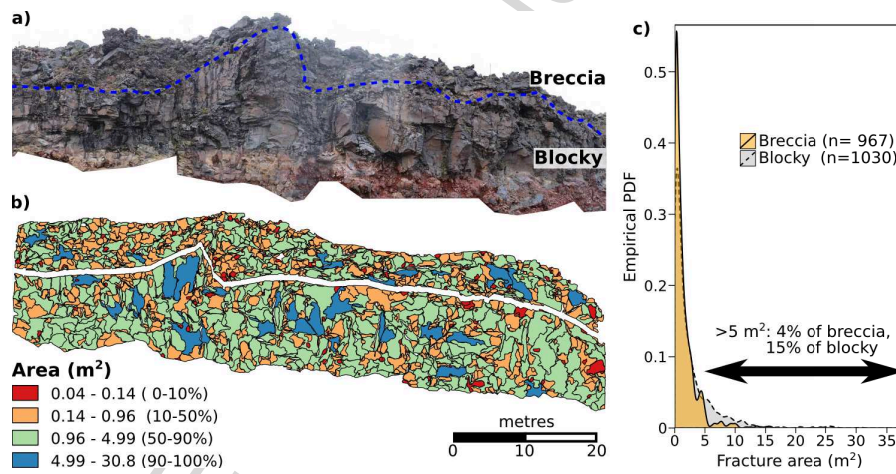
50

Figure 9: Variation of fracture area between the blocky and upper brecciated zones at the northern end of the outcrop. a) Panoramic photograph. b) TLS-processed fractures coloured by fracture area, with the percentage of fractures falling into each category indicated in brackets. The brecciated and blocky zones are separated by a white band to help visualisation. c) Empirical PDF of the fracture area in the breccia and blocky zones.
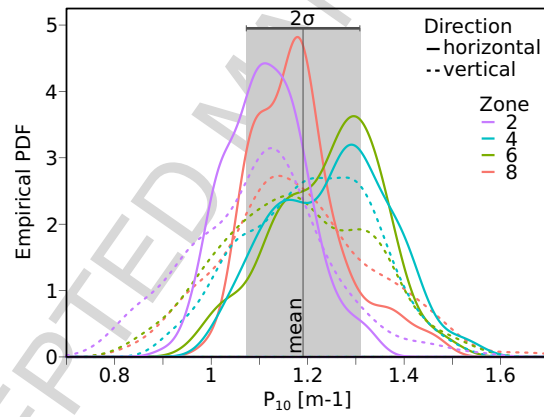
Figure 10: Empirical PDF of linear fracture density (P_{10}) along a series of virtual scanlines in zones 2; 4; 6 and 8 (Figure 7), measured every 10 cm parallel (sub-horizontal) and perpendicular (sub-vertical) to the lower breccia. Sub-horizontal scanlines have a mean fracture density of $1.2\,\mathrm{m}^{-1}$ and standard deviation of $0.1\,\mathrm{m}^{-1}$ (σ), shaded in grey.
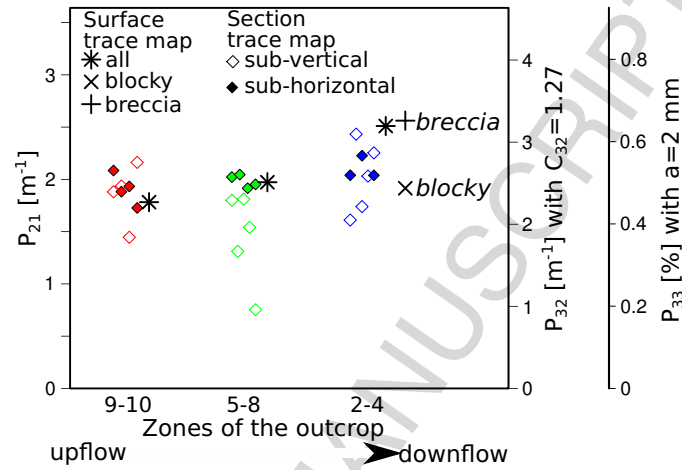
Figure 11: Measured P_{21} (areal intensity) and estimated P_{32} (volumetric intensity) and P_{33} (fracture porosity) parameters for each zone of the outcrop. Measurements are made over the entire outcrop surface (*Surface trace map*; Equation 2), and on trace maps perpendicular (sub-vertical) and parallel (sub-horizontal) to the lower breccia (*Section trace map*; Equation 3). P_{32} and P_{33} parameters assume $C_{32}=1.27$ and aperture$=2\,\mathrm{mm}$ (Equations 4 and 5). Zone numbers refer to Figure 7a; zones 2–4 measured on surface trace maps are subdivided by facies (breccia or blocky).
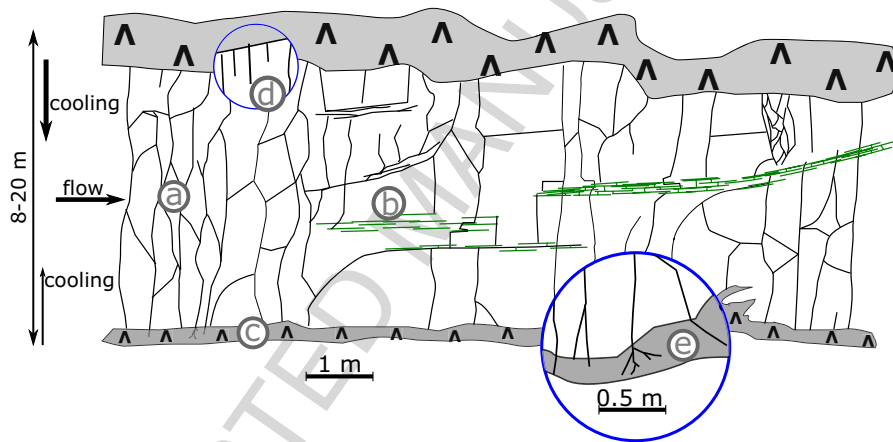
Tables

Figure 12: Interpretive diagram of the Happy Valley lava flow outcrop. (a) Column-forming fractures are well connected within the blocky zone, with higher areal density P_{32} for fractures perpendicular to the lower breccia than for those parallel to the flow direction. (b) Metre-scale zones of high fracture density are associated with platy fractures (green lines). (c) The high-porosity and friable breccias (shaded in grey) are partially connected to the blocky flow interior by those column-forming fractures that propagate into the breccia. The circled areas are zoomed-in views of the breccia-blocky interface showing (d) the higher density of column-forming fractures (commonly observed in lava flows, but inferred at Happy Valley due to the lack of exposure) and (e) the fracture bifurcations in the breccias.
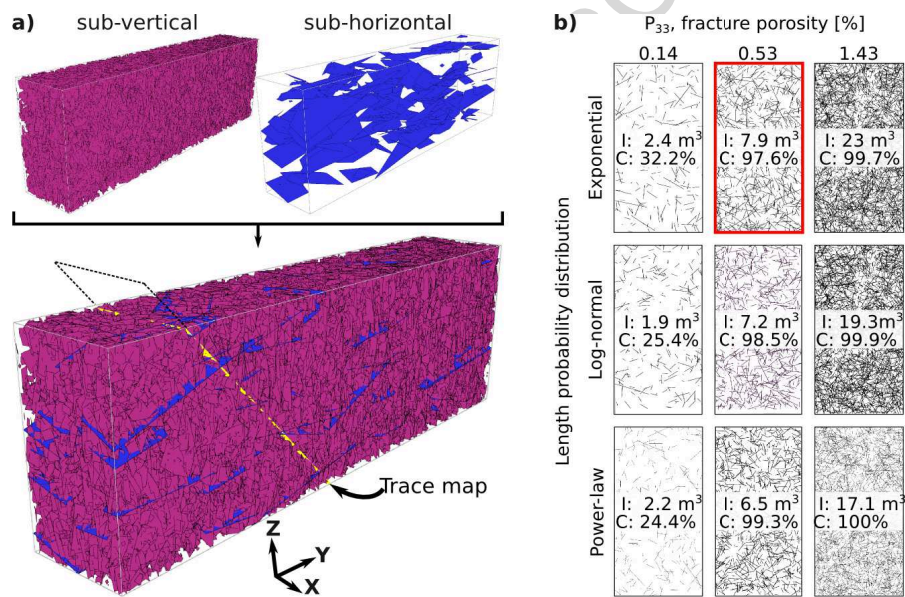
54

Figure 13: Examples of DFN models. a) DFN models are composed of two fracture sets (sub-vertical and sub-horizontal), with a 10:1 ratio of areal intensity P_{32}, in a volume of $36\,366\,\mathrm{m}^3$ (dimensions $15\times86\times28\,\mathrm{m}$). The trace map is a plane dipping $45°$ which samples the fractures intersecting the plane. b) Trace maps showing the intersection of the fractures with the trace map plane with various fracture length probability distributions and fracture porosity (P_{33}). I indicates the total volume of fracture intersecting the trace map, and C the fracture volume connected to the trace map as a percentage of the entire fracture network. The model generated with the parameters best characterising the Happy Valley outcrop (exponential length distribution and $0.53\,\%$ P_{33}) is outlined in red.

Table 1: Geometrical parameters of column-forming fractures measured from scanline and TLS-processed datasets, and parameters used to model DFN models (Figure 13). Length is presented as minimum/median/maximum values. *n: number of fractures per set.*

Parameter	Data	Column-forming fracture set		
		steeply dipping	intermediate	gently dipping
n	scanline	149 (335*)	18 (37*)	25 (107*)
	TLS	2622	610	171
Orientation	scanline	dip >55°	dip 30–55°	dip <30°
	TLS	dip >55°	dip 30–55°	dip <30°
	DFN+	m=000°/05°, sd=180°/05°		m=000°/70°, sd=180°/15°
Length [m]	scanline	0.03/0.65/11.6		
	TLS	0.14/1.00/9.31		
Area [m²]	TLS	0.05/1.02/46.42		
Radius [m]	TLS	Ex ($\frac{1}{\lambda}$=0.5)		
	DFN	Ex ($\frac{1}{\lambda}$=0.5); LN ($\bar{y}$=0.4, y_σ=0.75); PL (x_{min}=0.65, α=4)		Ex ($\frac{1}{\lambda}$=0.5); LN ($\bar{y}$=0.4, y_σ=0.75); PL (x_{min}=0.65, α=4)
P_{10} [m^{-1}]	scanline	1.5 (3.4*)	0.2 (0.4*)	0.2 (1.1*)
	TLS	1.2		
P_{21} [m^{-1}]	TLS	1.9		
P_{32} [m^{-1}]	TLS	2.4		
	DFN	0.65; 2.4; 6.5		0.065; 0.24; 0.65
Termination probability [0–1]	scanline	0.75		
	DFN	0.75		
Aperture [m]	DFN	No (m=0.002, x_σ=0.001)		No (m=0.002, x_σ=0.001)

*:After sampling orientation bias correction (Terzaghi, 1965)

+: Bivariate normal distribution, m=mean pole trend/plunge, sd=standard deviation trend/plunge

probability distributions: Exponential (*Ex*): $f(x) = \lambda \exp(-\lambda x)$; Log-normal (*LN*): $f(x) = \frac{1}{x ln(10) y_\sigma \sqrt{2\pi}} \exp\left[-\frac{1}{2}(\frac{log x - \bar{y}}{y_\sigma})^2\right]$; Power-law (*PL*): $f(x) = \frac{\alpha-1}{x_{min}}(\frac{x}{x_{min}})^{-\alpha}$; Normal (*No*): $f(x) = \exp\left[-(x-m)^2/2x_\sigma^2\right]/\sqrt{2\pi x_\sigma^2}$

Appendix A. TLS Processing Workflow

In this study, survey data were acquired using a Riegl LMS-Z420I terrestrial laser scanner and a Leica series 1200 RTK GPS. TLS devices emit a narrow laser pulse at a predefined vertical and horizontal angle and time, and subsequently detect the backscattered energy resulting from reflection off a surface. By rotating both horizontally and vertically the TLS can survey the target surface with an array of millions of measurements. The resulting 3-D point cloud is a survey-accurate measurement (± 10 mm Riegl, 2010) of the location (x, y, z) of points on the target surface relative to the TLS (Pfeifer & Briese, 2007; Buckley et al., 2008).

For this research, data was captured from three positions. Reflective cylindrical targets that are common to all TLS set ups were used to give orientation and aid combining the point clouds. The position of the TLS set ups and targets was determined using static GPS techniques with the base station mounted on a target for the duration of acquisition and the rover moved around the TLS set ups and other targets. With occupations of around 1 hour (less than what was used in this study), relative accuracies of ± 2 cm would be expected.

Merging and aligning ("registering") individual scans (Figure 4) involves positioning and orientating each TLS set up in an external reference frame. This is initially done using the surveyed coordinates of the set ups and targets. The alignment is further adjusted using Iterative Closet Point algorithms which define and match surfaces with the point clouds themselves. The rock surfaces at Happy valley were particularly suited to this approach and residuals from the adjustments were ~ 5 mm. At Happy Valley, the merged point cloud contains >6.3 million points, and few blind areas remain in the final dataset. Zones of the point cloud that captured vegetation or buildings were manually deleted in the CloudCompare v.2.7 software (CloudCompare, 2016). Finally, the merged scan was sub-sampled to ~ 1.4 million points with a 4 cm regular spacing from which fracture planes were extracted (Figure 2b). This point cloud was vectorised, with the calculation on each point of the normal to the best-fitting plane in a

local neighbourhood in CloudCompare (radius of 0.15 m; Figures 2b and A.1b).

The extraction of fractures from the TLS point cloud is performed using the Facets plugin in CloudCompare (Dewez et al., 2016, http://www.cloudcompare.org/doc /wiki/index.php?title=Facets_(plugin)). This method divides the point cloud into small planar patches using either a fast marching front propagation or a kd-tre, and then fuses those patches that are of similar orientation (as defined by the user) to generate fracture planes. The entire point cloud is then subdivided into a series of point sets (one per fracture plane) to which polygons are automatically fitted (Figure A.1b). The orientation (dip and dip direction) and size (area, horizontal and vertical length of the bounding rectangle) is automatically calculated for each polygon (Figures 5b and 2c-e). The fast-marching process better accommodated the curved fractures of the Happy Valley outcrop and was preferred to the kd-tree algorithm (Figure A.1d-e. The best set of parameters is listed in Table A.1.

The choice of parameters and validation of the fracture processing with the Facets plugin is made in three ways. Firstly, the spatial extent and orientation of fractures processed from the Facets plugin are compared to the manual scanline where available; secondly, the spatial extent of the processed fractures are compared to the Gigapan panoramic photographs over the whole outcrop; and thirdly, the delineation of fractures is compared to the results of the RansacSD shape detection algorithm in CloudCompare (Schnabel et al., 2007) on a subset of the outcrop. The RansacSD method involves four steps (Figure 4): (1) vectorisation with *SEFL* (García-Sellés et al., 2011), which calculates the normals to each point and computes local geometrical parameters; (2) filtering of points of low planarity and high collinearity, which correspond to fracture edges in *CloudCompare*; (3) application of the RansacSD algorithm, looking for planes and spheres, which segments the point cloud into a series of subsets of points; and (4) post-processing, to manually check each subset, and subdivide them as necessary to match scanline and Gigapan photographs observations. As described by Ferrero et al. (2009), the filtering of fracture edges (steps 1 and 2) was necessary to obtain good results in RansacSD: without filtering, RansacSD

generates very large fractures which requires significantly more post-processing, including removal of subsets generated along the fracture edges. The parameters used for the RansacSD step were iteratively selected by comparing the results to the scanline data and the Gigapan panoramas.

The RansacSD method has one major advantage compared to Facets: it detects spheres as well as planes, which allows the detection of curved fractures common in the Happy Valley outcrop. However, the additional steps of filtering fracture edges before running RansacSD, checking and modifying each subset individually, and fitting a plane to each subset to obtain the orientation and size of the fracture, is time-consuming. Conversely, the Facets method does not allow the delineation of curved fractures, but is significantly faster and provides results consistent with results from RansacSD, and from scanline and Gigapan photographs observations.

The regular resampling of the point cloud prior to the fracture extraction ensures that processing parameters are constant throughout the point cloud. Based on visual checks of processed fractures, a minimum of 25 points per fracture was imposed during the Facets processing to limit the false detection of noise as fracture planes. This threshold, equivalent to a fracture area of $0.04 \, \mathrm{m}^2$, is similar to that recommended by Sturzenegger & Stead (2009a), and means that fractures with lengths of $\sim < 0.2 \, \mathrm{m}$ are not sampled (for a square fracture).

Figure A.1b shows the orientation of the neighbourhood of each point (i.e. after vectorisation) and highlights the variations of dip and dip direction over a single fracture plane. These undulations are fitted by a series of spheres and planes by the RansacSD algorithm (Figure A.1c), and a series of planes by the Facets algorithm (Figure A.1d). Fracture orientations (dip magnitude and direction) of fractures measured on the manual scanline and using the Facets algorithm only differ by a few degrees in both dip magnitude and direction (see examples in Figure A.1), a discrepancy consistent with accuracies on TLS reported by Sturzenegger & Stead (2009a) and with errors on compass measurements.
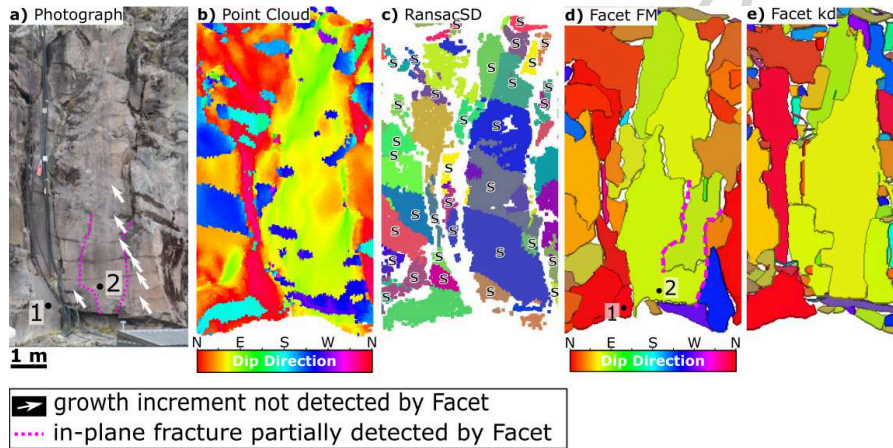
59

Figure A.1: Fracture processing of the TLS point cloud. a) Section of a Gigapan photograph acquired 100 m from the outcrop showing a column-forming fracture, with growth increments (white arrows) and in-plane fractures (purple dotted lines). b) TLS point cloud coloured by the local orientation. c) Point subsets separated with RansacSD. Fractures best fitted by a sphere are specified with an (S), others are recognised as planes. d) Planes delineated with Facets, fast-marching algorithm; parts of the in-plane fractures are recognised. e) Planes delineated with Facets, kd-tree algorithm. Fracture "1" is oriented 80°/353° and 80°/359° on the scanline and TLS-processed datasets, respectively; Fracture "2" is oriented 78°/070° and 82°/069° on the scanline and TLS-processed datasets, respectively.

Table A.1: Parameters used for the Facets plane extraction with the Fast-marching algorithm (used in the study) and kd-tree (Figure A.1e). In this case, an octree level of 10 is equivalent to a grid step of about 0.09 m.

Algo-rithm	octree level	maximum distance at 99 % [m]	minimum points per facet	maximum edge length [m]	maximum angle for cells fusion	maximum relative distance for cell fusion
Fast-marching	10	0.17	25	0.3	-	-
kd-tree	10	0.17	25	0.3	30	1

60

Supplementary data

High-resolution Panoramic Photographs

The high-resolution panoramic photographs are accessible on GNS Science's virtual media library (`https://vml.gns.cri.nz`; photographs number 181972-181974). Enlargeable versions of the four panoramic photographs used in this study are also available at: `www.gigapan.com/gigapans/191973`;

`www.gigapan.com/gigapans/e1911e3d60bda65464de404762ff36b0`;

`www.gigapan.com/gigapans/b7deaec44afe77fab919b671617b19bc` and

`www.gigapan.com/gigapans/6fe29b5bc96c857ae365fb646ace5e84`.

Fracture Radius Parameters

Fracture radius parameters estimated from trace map analysis of the TLS-processed dataset are presented in Table A.3.

Table A.3: Parameters (mean and 1 standard deviation) of the probability distribution fitted to the fracture radius from sub-horizontal and sub-vertical trace maps (i.e. parallel and perpendicular to the lower breccia, respectively), and near the manual scanline. *n: number of scanline per zone, as defined in Figure 7.*

Direction	Zone	n	Distribution				
			Exponential	Log-normal		Power-law	
			$1/\lambda$	$\bar{y}$	y_σ	x_{min}	$D=(\alpha\text{-}1)$
sub-horizontal	2–4	3	0.5±0.1	0.8±0.1	0.4±0.1	0.7±0.1	4.0±0.1
	5–8	4	0.5±0.1	0.7±0.1	0.4±0.1	0.6±0.1	3.9±0.1
	9–10	3	0.5±0.1	0.7±0.1	0.5±0.1	0.6±0.1	3.7±0.2
	2–10	10	**0.5±0.1**	**0.7±0.1**	**0.4±0.1**	**0.6±0.1**	**3.9±0.2**
sub-vertical	2–4	5	0.5±0.1	0.8±0.2	0.4±0.1	0.7±0.2	3.9±0.1
	5–8	5	0.6±0.05	0.8±0.1	0.5±0.1	0.7±0.1	3.7±0.2
	9–10	5	0.6±0.1	0.8±0.1	0.5±0.1	0.7±0.1	3.7±0.2
	2–10	15	**0.6±0.1**	**0.8±0.2**	**0.5±0.1**	**0.7±0.1**	**3.8±0.2**
along scanline	8–10	1	0.5	0.8	0.4	0.7	3.8